Dipl.-Ing. Alida Nooke

Gas Detection by Means of Surface Plasmon Resonance Enhanced Ellipsometry

BAM-Dissertationsreihe · Band 89
Berlin 2012

Die vorliegende Arbeit entstand an der BAM Bundesanstalt für Materialforschung und -prüfung.

Impressum

Gas Detection by Means of Surface Plasmon Resonance Enhanced Ellipsometry

2012

Herausgeber:
BAM Bundesanstalt für Materialforschung und -prüfung
Unter den Eichen 87
12205 Berlin
Telefon: +49 30 8104-0
Telefax: +49 30 8112029
E-Mail: info@bam.de
Internet: www.bam.de

Copyright © 2012 by
BAM Bundesanstalt für Materialforschung und -prüfung

Layout: BAM-Referat Z.8

ISSN 1613-4249
ISBN 978-3-9815134-4-8

Gas Detection by Means of Surface Plasmon Resonance Enhanced Ellipsometry

vorgelegt von
Diplom-Ingenieurin
Alida Nooke

von der Fakultät III – Prozesswissenschaften
der Technischen Universität Berlin
zur Erlangung des akademischen Grades

Doktor der Ingenieurwissenschaften
- Dr.-Ing. -

genehmigte Dissertation

Promotionsausschuss:
Vorsitzender: Prof. Dr. G. Tsatsaronis
1. Berichter: Prof. Dr. J. Steinbach
2. Berichter: Dr. A. Hertwig

Tag der wissenschaftlichen Aussprache: 16.03.2012

Berlin 2012

Abstract

This thesis investigated gas sensing by means of surface plasmon resonance enhanced ellipsometry. Surface plasmons were excited in a 40 - 50 nm gold layer by a He-Ne-laser using the Kretschmann configuration, which was arranged on a self-made copper measuring cell. A fixed angle of incidence and the ellipsometric parameter Δ as the measured value were used to monitor changes in the gas phase. Different types of gases were investigated: flammable (hydrocarbons and hydrogen), oxidising (oxygen and ozone), toxic (carbon monoxide) and inert (helium and nitrogen). The gas types can be distinguished by their refractive indices, whereas the sensor responds instantly relative to the reference gas with an increase or a decrease in Δ. Diluting the analyte gas with a reference gas (nitrogen or air) allowed the detection limits to be determined, these lay in the low % range. The sensor stability was also enhanced as well as the sensitivity by modifying the gold layers with a 3-10 nm additional layer. These additional layers consisted of the inorganic materials TiO_2, ZrO_2, MgF_2 and $Fe : SnO_2$ which were deposited by different coating processes. Surface investigations were made of every utilised layer: scanning electron microscope and atomic force microscope measurements for surface topology and spectroscopic ellipsometry mapping to determine the optical constants and the layer thicknesses. All applied materials protected the gold layer from contaminations and thus prolonged the life span of the sensor. Furthermore, the detection limits were reduced significantly, to the low ppm range. The material $Fe : SnO_2$ demonstrates a special behaviour in reaction with the toxic gas carbon monoxide: Due to the iron doping, the response to carbon monoxide is extraordinary and concentrations below 1 ppm were detected. In order to approach a future application in industry, the sensor system was adapted to a stainless steel tube. With this measuring arrangement, pulse and pressure experiments could be performed. The probable mechanisms occuring at the sensor surface and feasible applications in the future are discussed in this thesis.

Keywords: gas sensor, ellipsometry, surface plasmon resonance effect, TiO_2, ZrO_2, MgF_2, $Fe : SnO_2$

Zusammenfassung

In dieser Arbeit wurde der Nutzen von Ellipsometrie in Kombination mit Oberflächenplasmonenresonanz an 40 - 50 nm Goldschichten als Sensorsystem für sicherheitstechnisch relevante Gase untersucht. Eine Kretschmann Konfiguration bestehend aus einem BK7 Glasprisma und einem mit dem Gold beschichteten BK7 Glasplättchen wurde auf einer Kupfermesszelle platziert, durch welche die Gase mit definiertem Volumenstrom geleitet wurden. Untersucht wurden verschiedenste Gase: entzündliche wie Kohlenwasserstoffe und Wasserstoff, oxidierende wie Sauerstoff und Ozon, toxische wie Kohlenmonoxid und inerte wie Helium und Stickstoff. Durch Einstellen eines festen Einfallswinkels und unter Benutzung des ellipsometrischen Parameters Δ als Messgröße konnten geringste Änderungen in der Gasphase detektiert werden. Die reinen Gase konnten anhand ihres Brechungsindexes unterschieden werden, wobei die Änderung der Gasatmosphäre in Δ einen Anstieg bzw. Abfall relativ zum Referenzgas (Luft oder Stickstoff) hervorrief. Die Analytgase wurden mit dem Referenzgas zu kleineren Konzentrationen gemischt und so die Nachweisgrenzen bestimmt, welche im niedrigen %-Bereich lagen. Zur Verbesserung des Sensors bezüglich der Langzeitstabilität wurden die Goldschichten zusätzlich mit 3 - 10 nm anorganischem Material (TiO_2, ZrO_2, MgF_2 bzw. $Fe : SnO_2$) beschichtet. Jede Schicht wurde mittels Rasterelektronenmikroskopie sowie Rasterkraftmikroskopie untersucht um Aufschluss über die Oberflächenbeschaffenheit zu erhalten. Mittels spektroskopischer Ellipsometrie wurden die optischen Konstanten sowie die Schichtdicken bestimmt. Alle Zusatzschichten schützten die Goldschicht vor unerwünschten Kontaminationen und verlängerten so die Lebensdauer des Sensors. Außerdem konnten die Nachweisgrenzen deutlich verbessert werden, welche mit den Zusatzschichten im unteren ppm-Bereich lagen. Eine besondere Eigenschaft konnte bei $Fe : SnO_2$ beobachtet werden: durch die Eisendotierung ist das Material besonders sensitiv gegenüber dem giftigen Gas Kohlenstoffmonoxid, so dass Konzentrationen unter 1 ppm nachgewiesen werden konnten. Im Hinblick auf eine zukünftige industrielle Nutzung wurde dieses Sensorsystem an ein handelsübliches Rohr montiert, um so Puls- sowie Druckmessungen durchzuführen. Die potentiell ablaufenden Mechanismen an der Sensoroberfläche und denkbare zukünftige Anwendungsmöglichkeiten wurden diskutiert. In dieser Arbeit konnte gezeigt werden, dass Ellipsometrie in Kombination mit Oberflächenplasmonenresonanz als sensitive, schnelle Sensormethode zur Gasmessung genutzt werden kann und dass das Potenzial zu einer industriellen Nutzung gegeben ist.

Schlagwörter: Gassensor, Ellipsometrie, Oberflächenplasmonenresonanzeffekt, TiO_2, ZrO_2, MgF_2, $Fe : SnO_2$

Acknowledgement

Ein besonders herzliches Dankeschön geht an Herrn Prof. Dr. Jörg Steinbach, den ich für die Betreuung meiner Promotion gewinnen konnte und den ich wegen seiner Fachkompetenz und seines Charakters sehr schätze.

Besonderer Dank gilt ebenso meinem Projektleiter und Zweitkorrektor Herrn Dr. Andreas Hertwig, dem meine Arbeit ein persönliches Anliegen war, der mich hervorragend fachlich betreut hat und mich auch sonst in jederlei Hinsicht jederzeit unterstützt hat. Danke für die vielen Tipps, Ratschläge, Erklärungen und Hilfestellungen!

Ganz besonders möchte ich mich bei meinen Teamkollegen Andreas Krause und Dr. Hannes Krüger bedanken. Sie haben mir nicht nur mit Rat und Tat während des Projekts zur Seite gestanden, sondern auch darüber hinaus z. B. in der Diskussion und Gegenlesen meiner Arbeit und haben mir immer wieder ihre Loyalität als echte Freunde bewiesen. Danke für zahlreiche fruchtbare Gespräche auch nach Beendigung des Projekts, eure Ideen, eure moralische Unterstützung. Ohne euch hätte ich es nie geschafft!

Bei Herrn Dr. Volkmar Schröder und Herr Dr. Volkmar Lohse möchte ich mich für die Einstellung in das Projekt und das entgegengebrachte Vertrauen bedanken. Herrn Dr. Lohse habe ich als kompetenten, fairen, hilfsbereiten Arbeitsgruppenleiter zu schätzen gelernt, der immer ein offenes Ohr für seine Mitarbeiter hat.

Bei den Mitgliedern meiner Arbeitsgruppe, Jörg Bethge, Gerd Buschbeck, Detlef Negendank und Thomas Runge möchte ich mich herzlich bedanken. Egal wann und mit welchem Problem, ich wurde sofort tatkräftig unterstützt.

Ebenso möchte ich mit bei Herrn Dr. Uwe Beck bedanken, für sein großes Interesse an meinem beruflichen Erfolg, die Unterstützung des Projekts, bei Veröffentlichungen und bei Präsentationen mit Ideen und Ratschlägen und für die fruchtbaren, aufbauenden Gespräche. Der gesamten Arbeitsgruppe um Dr. Uwe Beck schulde ich Dank für die Integration in die Gruppe vor allem bei Feierlichkeiten aller Art. Danke an Matthias Weise für die Herstellung der Schichten und der zahlreichen weiterführenden fachlichen Diskussionen, danke ebenso an Mario Sahre für die AFM Messungen.

Mein Dank geht auch an Herrn Dr. Martin Kormunda von der J. E. Purkinje University in Ústí nad Labem mit dessen Hilfe ein gemeinsamer Fachartikel entstanden ist.

Herrn Dr. Thomas Schendler möchte ich danken für das Interesse an meinem persönlichen Werdegang und die Unterstützung bei meiner Berufsfindung.

Des Weiteren gilt mein Dank der gesamten Arbeitsgruppe um Dr. Kai Holtappels, die stets für eine nette Atmosphäre gesorgt hat und mich bedingungslos in die Mittags- und Kaffeerunde integriert hat. Besonders für die fachlichen Diskussionen und offenen Ohren für allerlei Probleme geht mein Dank an Dr. Kai Holtappels, Dr. Enis Askar und Ronald Meyer.

Danke an Dr. Karim Habib für die vielen nützlichen Tipps vor allem für LaTeX.

Bedanken möchte ich mich weiterhin bei Frau Dr. Marianne Nofz für die fachkundige Unterstützung bei der Schichtenherstellung.

Danke auch an Frau Dr. Natascha Schelero für die Hilfestellung bei der LB Beschichtung.

Special thanks to Dr. Přemysl Maršik for correcting my physics.

Herzlichen Dank an Nora Adwan für die schnelle und gründliche Englisch Korrektur.

Bedanken möchte ich mich auch bei meiner gesamten Familie, die immer an mich geglaubt hat, vor allem mein Bruder Raoul Nooke, der mir oft mit seiner nüchternen Art den rechten Weg gewiesen hat.

Contents

1 Introduction

Sensing gases and the determination of gas concentrations is important in several areas of life. Certain gases, in defined concentrations, can cause immense damage, for example through explosions or the death of human beings. Gas sensors are important equipment e.g.in the chemical industry: The concentration of pollutant gases (e.g. sulphur dioxide and nitrogen oxides) has to be determined in oil drilling and refineries, in the steel industry or wastewater treatment. Toxic gases (e.g. carbon monoxide or hydrogen sulphide) have to be determined in very low concentrations in order to warn persons working in metal and coal mines. Ecologically harmful gases (e.g. carbon dioxide or ozone) need to be detected for environmental monitoring or in the automobile industry. Explosive or flammable gases (e.g. hydrocarbons or hydrogen) are to be determined below their lower explosive limit (LEL) in oil rigs or refinery and drilling sites. Devices for sensing gas are utilized in the private sector as well, e.g. in apartment buildings (domestic gas), hospitals (oxygen), or tunnels (automotive exhaust emissions) [1]. Requirements for gas sensors are fast detection, distinction between gas types and chemical and physical stability.

Nowadays, a large number of commercial gas detecting devices are on the market for a variety of applications. The basic principle is to transform chemical information (e.g. concentration) into an analytically useful signal (e.g. voltage) [2]. There are among others catalytic or metal oxide semiconductor gas sensors based on the resistance change of platinum or a metal oxide after the catalytical reaction of gases. Furthermore, electrochemical sensors based on the principle of galvanic cell or optical gas sensors have been developed. Optical sensors are widely used for the detection of flammable gases due to their absorption bands in the infrared region (IR sensors). In addition, optical sensors based on the surface plasmon resonance (SPR) effect are known. Today, SPR sensors are commercially used in biochemistry for the detection of

liquid analytes [3]. Gas detection was carried out by means of the SPR effect in 1982 [4], but no commercial device has been developed.

A SPR sensor usually consists of a glass prism with a metallic layer, where surface plasmons are excited by a light beam. The p-polarised part of the light interacts with the metal, the electrons of the metal begin to oscillate and the resulting quasi particle is called surface plasmon (SP) [5]. Marginal changes on the metal surface, such as the adsorption of molecules, disturb this oscillation and the change in the intensity of the reflected light dependent on the wavelength or the angle of incidence can be quantified. Changes in the polarisation can also be detected as these are determined by changes in the light intensity [6]. This can be done with SPR enhanced ellipsometry (SPREE) [7]. By means of ellipsometry, the parameters Ψ ($\tan\Psi$ represents the ratio of s- and p-polarised part of a light wave) and Δ (phase difference between s-and p-polarised part of a light wave) are determined upon reflection dependent on the angle of incidence (AOI). The SPR effect is accompanied by a minimum in the Ψ-AOI spectrum and a huge dip in the Δ-AOI spectrum. The AOI-spectra are affected by any change in the refractive index, e.g. when the concentration of the analyte medium changes.

In this work, the principles and applications of sensing gas by means of SPREE are investigated. The advantage of this method is the possibility of measuring the gas concentration from the outside. This means on the one hand an easy adaption to apparatus like tubes or vessels, on the other hand no additional component meaning a possible interference factor for the process. The basic sensor layer in this work is gold modified by top-coating. Several materials for top-coating the gold in order to enhance the stability and the sensitivity of the sensor system will be examined. Possible explanations for the sensing mechanisms are considered, supported by surface analysis of the materials and gas sensing experiments. The advantages and disadvantages of using a gas sensor based on SPREE and a probable application possibility in industry are discussed.

Part I

Theory and experimental details

2 Theory

The following chapter will give an overview of commercial gas sensors, insight into the physical background of ellipsometry, the optical method used for read-out as well as for surface analysis, and the special case of surface plasmon resonance enhanced ellipsometry.

2.1 Commercial gas sensors

Devices for detecting and warning of hazardous gases are omnipresent in industry and non-industrial fields: gas concentrations must be registered e.g. in chemical industries, near oil drillings and in refineries, in steel industry, for environmental monitoring, for combustion control, in wastewater treatment, in metal or coal mines, in the field of biotechnology, in hospitals, automobiles, or private domiciles [1, 5]. According to the International Union of Pure and Applied Chemistry (IUPAC), a sensor is defined as follows: "A chemical sensor is a device that transforms chemical information, ranging from the concentration of a specific sample component to a total composition analysis, into an analytically useful signal. The chemical information, mentioned above, may originate from a chemical reaction of the analyte or from a physical property of the system investigated." Since there are lots of different types of gas sensors based on various different mechanisms, it is necessary to classify them. They could be e.g. classified according to detected gases or fields of application. The

IUPAC classifies them according to sensing mechanism [2]:

- Optical: changes of optical phenomena like absorbance, reflectance, luminescence, fluorescence, refractive index (including surface plasmon resonance effect), optothermal effect or light scattering are measured
- Electrochemical: the electrochemical interaction between analyte and electrode is used, as in voltammetric, potentiometric sensors and potentiometric solid electrolyte gas sensors, and chemically sensitized field effect transistor (CHEMFET)
- Electrical: change of electrical properties is measured as in metal oxide semiconductor, organic semiconductor, electrolytic conductivity and electric permittivity sensors
- Mass sensitive: based on change in mass as in piezoelectric or surface acoustic wave sensors
- Magnetic: change of paramagnetic properties is detected and mostly used in oxygen sensors
- Thermometric: heat effects of a chemical reaction or adsorption as in catalytic sensors are quantified
- Other sensors based on physical properties such as radiation

The requirements for gas sensors are obvious: they have to be sensitive to low gas concentrations. The degree of sensitivity depends e.g. on the lower explosion limit (LEL) or the toxicity of the gas. For example, 4 % (v/v) (which is the LEL) of the explosive gas hydrogen must be detected in chemical industries and even 0.5 ppm must be detected in refineries and drilling sites [1]. Furthermore, gas sensors should have a response time as short as possible. The often used term is t_{90}: the time until 90% of the final signal is reached [8–10].

The most important gas sensor types used in industry are described below.

Catalytic sensors They are cost-effective sensors for detecting combustible gases in the field of explosive protection. The measuring element is the pellistor, that consists of an electrically heated (up to 250 ℃) platinum spiral coil, coated with alumina and an outer layer of thorium oxide substrate with a palladium or rhodium catalyst. The analyte gas is oxidised on the surface of the sensor and thus the temperature and the resistance of the platinum change. By using the spiral coil as a thermometer and a wheatstone bridge the change in resistance can be directly related to the gas concentration. The disadvantage of this kind of sensors is the danger of catalyst poisoning by silicones, sulphur or lead compounds [5].

Metal oxide semiconductor (MOS) sensors An important type of sensor within the electrical devices are made of semiconductive materials, normally oxides of the transition or heavy metals, e.g. tin or indium. The gas molecules are adsorbed by the heated surface (200-400 ℃) and catalytically oxidized which leads to a change in the electrical resistance of the oxide material [11]. There are reducing gases that transfer electrons to the material (e.g. hydro carbons, carbon monoxide, or alcohols) and oxidising gases that accept electrons from the material (e.g. nitrogen oxide, chlorine, or oxygen). Above 100 ℃ oxygen ions are chemisorbed at the surface of the semiconductor either in molecular or atomic form at which above 150 ℃ the atomic form dominates [12]. In the case of carbon monoxide it is oxidised with an oxygen ion adsorbed at the surface in atomic form (O_S^-) to carbon dioxide:

$$CO + O_S^- \longrightarrow CO_2 + e^- \tag{2.1}$$

and the free charge increases the conductivity. In case of molecules with hydrogen atoms water is generated, too [13]:

$$2NH_3 + 7O_S^- \longrightarrow 2NO_2 + 3H_2O + 7e^- \tag{2.2}$$

The main field of application for semiconductor sensors is safety management

where explosive gas - air - mixtures must be detected in the region of the LEL. The exact value reading of the concentration and selectivity are not as important as quick response. To develop the sensor with regard to selectivity, materials are varied and doped with other metals [14].

Optical sensors Infrared (IR) sensors are the most common sensors based on optical measurement. They are used to detect flammable gases due to their absorption bands in the IR region. Two light beams, one with the wavelength matching the absorption peak of the analyte gas and one reference beam are sent through the gas atmosphere and reflected back to the device where the detector compares the signal intensities and calculates the gas concentration. This kind of sensor is fast, highly selective, and not sensitive to catalyst poisoning, temperature, or pressure and moisture fluctuation, but IR inactive gases like hydrogen cannot be detected [14].

Another type of optical sensor is based on the SPR effect. In the late seventies it was used first for monitoring [3] and in the early eighties its potential usefulness in gas detection was investigated [4]. Nowadays, optical sensors based on the SPR effect are commercially used and widely applied in the field of biochemistry: For the investigation of biomolecular interactions and the detection of chemical and biological analytes [3]. Different methods for optical excitation of SPR waves are known: total reflection (prism coupling) or diffraction on periodic metallic gratings (grating coupling). SPR sensors are made of a prism with a metallic layer and a resonance layer (usually polymers or biomolecule layers). A light beam coming from the glass side goes through total reflection and interacts with the metallic layer. A resonance with the surface plasmons (SP) results and part of the light energy is absorbed (see Section 2.3) [5]. The resonance conditions of the SPs are affected by a change in the refractive index of the analyte medium, hence the intensity of reflected or diffracted light or its wavelength or angular spectrum is detected by charge - coupled device (CCD) arrays or photodiode arrays. Concerning gas analysis, mainly NO_2 detectors with phthalocyanin layers are used [5], but the detection of other gases have been reported in literature as well: NO [15] and H_2S [16] or vapours like methanol [17] have been detected. The detection limit of SPR

sensors is often declared in refractive index units (RIU), i.e. the lowest relative change in the index of refraction Δn, which can be measured [18, 19].

Electrochemical sensors Most toxic gases like carbon monoxide, dihydrogen sulphide, chlorine or sulphur dioxide can be detected through the application of electrochemical sensors. This type of sensor has a good linearity and a long operating lifetime. There are two different basic types: Potentiometric sensors which measure voltage and amperometric sensors which measure electric current. In potentiometric constructions the principle of galvanic cells, which consists of a measuring electrode and a reference electrode connected by a salt bridge, is used. The potential of the cell is given by the Nernst equation:

$$Q = Q_0 \pm \frac{0.059}{z_i} log a_i \tag{2.3}$$

where Q_0 is the standard reduction potential, z_i is the ion's valence and a_i is the activity of the measured ion. In case of a cation, the algebraic sign is positive, in case of an anion it is negative. The gas diffuses through a membrane into the cell and comes in contact with the electrode. Depending on the type of cell, the analyte gas is oxidised or reduced at the measuring electrode and the potential changes relative to the reference electrode [5].

In amperometric cells a voltage is given at the electrode and the resulting electric current is measured. Amperometric cells consist of a working electrode and a counter electrode. Here the measured value is the diffusion current [14]. In sensors based on an amperometric measuring principle, the response time is lower than in potentiometric cells, due to the fact that the electrode does not have to be in thermodynamic equilibrium with the analyte and thus the time of thermalisation does not matter. Since amperometric sensors can be easily miniaturised and inexpensively produced, they are used more often than potentiometric sensors.

Another group of electrochemical sensors is based on the metal oxid semiconductor field-effect transistor (MOSFET). Normally, MOSFETs are used with three electrodes: source, gate and drain and can be applied as sensor for liq-

uids. They are often named chemical FET (CHEMFET) or ion sensitive FET (ISFET). If MOSFETs are constructed with only two electrodes, they can be used as gas sensor due to the different conductivities. MOSFETs are usually built of a semiconductor, e.g. p-doped silicium, covered with an isolatic layer such as silicium oxide which is metallized with a thin metallic layer, often gold. Bulk, insulating layer and gate build a condensator which is controlling the current between source and drain. The analyte affects the resistence of the MOSFET [5].

2.2 Ellipsometry

Ellipsometry is a nondestructive and sensitive optical measuring method mostly used for the analysis of thin films. The change in the polarisation state of a light beam on a sample is measured after beeing reflected. By applying an adequate model, the optical constants (refractive index n and extinction coefficient k) and the thickness d - also of multi layer systems - can be determined [20]. In this work, ellipsometry has been used for read - out of the surface plasmon resonance (SPR, see Section 2.3). In the following sections, a background to understanding ellipsometry and its physical principles will be introduced.

2.2.1 Optical constants n,k and dielectric function ϵ

The refractive index becomes relevant when an electromagnetic wave hits an interface between two optically different media and is defined as the ratio of the velocity of light in a vacuum to the same in media:

$$n = c/v \tag{2.4}$$

where c is the velocity of electromagnetic waves in vacuum (known as a constant value of $2.99792 \cdot 10^8$ m/s) and v the velocity in the corresponding medium.

As long as the media are transparent, i.e. there is no energy absorption, the

index of refraction is a real number. The modification of the electromagnetic wave, when passing the interface, occurs only in a change of wavelength λ, not in the frequency f (photon energy E_f). In case of absorbing media, the wavelength changes and the index of refraction becomes a complex number which is defined as:

$$N = n - ik = \sqrt{\epsilon} \tag{2.5}$$

with the complex function ϵ:

$$\begin{aligned} \epsilon &= \epsilon' - i\epsilon'' \\ \epsilon' &= n^2 - k^2 \\ \epsilon'' &= 2nk \end{aligned} \tag{2.6}$$

where k is the extinction coefficient and ϵ is the dielectric function or permittivity. The latter describes the ability of a medium to generate dielectric polarisation P: any material responds to an external electric field by reorientating the charges (e.g. electrons, protons or ions), and different kinds of polarisation can occur:

- orientational polarisation: uniform orientation of partial charges in polar molecules like water
- electric polarisation: induced dipoles by displacement of the electrons relative to the nucleus in nonpolar molecules like carbon dioxide
- ionic or atomic polarisation: induced dipoles by displacement of positive ions relative to negative ions in crystals like sodium chloride

The response of the charges to the external electric field is described by the dielectric function [20]:

$$\epsilon = 1 + \frac{P}{\epsilon_0 E} = 1 + \chi \tag{2.7}$$

where ϵ_0 is the dielectric constant in vacuum, and χ the dielectric susceptibility. The charges follow the external electric field (e.g. incident light) and since it is alternating, the direction of orientation changes quickly, the charges begin to oscillate and electric dipole radiation occurs. This radiation slows the propagation velocity of the incident light and for that reason the index of refraction can be expressed by the dielectric function (see Equation 2.5). The dielectric function is dependent on the frequency of the incident light, because different kinds of polarisation are excited by accordant frequencies. There is thus no constant value of a material, but a function varying with the frequency of the incident light. In many cases, the dielectric function of a multi-layer sample is modeled (see Section 2.2.4) in order to determine the optical constants [20].

2.2.2 Polarisation of light

Light is a transverse electromagnetic wave consisting of the electric field $\vec{E}$ that oscillates perpendicular to the magnetic field or magnetic induction $\vec{B}$. Transverse means that the oscillation is perpendicular to the direction of propagation. The space-time dependency of an electromagnetic plane wave can be described in general as:

$$\vec{E}(\vec{r},t) = \vec{E}_0 \cos(\omega t - \vec{K} \cdot \vec{r}) \tag{2.8}$$

with the amplitude $\vec{E}_0$, the angular frequency $\omega = 2\pi\mathrm{f}$ and the wave vector $\left|\vec{K}\right| = \mathrm{n}2\pi/\lambda$ determining the direction of propagation. In order to distinguish it from the extinction coefficient k, the wave vector is always written as capital K in this work.

In light emitted by most of the natural radiation sources, the oscillation of the electrical field is randomly distributed in all directions, it is then unpolarised. If the electric field of a transverse wave oscillates in a certain direction, this is known as polarisation. The expression is not to be mistaken for dielectric polarisation explained in Section 2.2.1. The degree of polarisation specifies the fraction of polarisation in the light wave. Assuming that a light beam reflected on a surface has certain directions of oscillation of the electric field, one

part of the electric field oscillates parallel to an imaginary plane of incidence. This is the p-polarised (from the german parallel) or transverse magnetic (TM) part of the wave, the part oscillating perpendicular to the plane of incidence is called s-polarised (from the german senkrecht) or transverse electric (TE) [21]. These two orthogonal optical oscillations can be described as:

$$\vec{E}(\vec{r},t) = \vec{E}_0^p \cos(\omega t - \vec{K} \cdot \vec{r} + \delta_p) \tag{2.9}$$

and

$$\vec{E}(\vec{r},t) = \vec{E}_0^s \cos(\omega t - \vec{K} \cdot \vec{r} + \delta_s) \tag{2.10}$$

with the initial phases $\delta_{p,s}$. By superimposing these two polarised plane waves, every polarisation state of the whole wave can be described as:

$$\vec{E}(\vec{r},t) = \vec{E}_0^p \cos(\omega t - \vec{K} \cdot \vec{r} + \delta_p) + \vec{E}_0^s \cos(\omega t - \vec{K} \cdot \vec{r} + \delta_s) \tag{2.11}$$

As described often in literature [20–22] the electromagnetic wave is regarded in front view and the resulting vector $\vec{E}$ is considered in the p-s-plane perpendicular to $\vec{K}$ (see Figure 2.1). The resulting vector is dependent on the amplitudes and phases of the single vectors. In general, it rotates clockwise or counter clockwise and changes its magnitude. Its ending point describes an ellipse on the p-s-plane and thus the light is referred to as elliptically polarised.

A special case occurs when the phase difference is 0, π or 2π. The resulting vector is then linear, thus the wave is linearly polarised. Another special case is when $E_0^s = E_0^p$ and the phase difference is $\pi/2$ or $3/2\pi$: the resulting vector $\vec{E}$ describes a circle, the light is circularly polarised. In ellipsometry measurements the amplitude ratio and the phase difference between s- and p-polarised waves of a light beam reflected on a sample is determined. The name ellipsometry refers to the generally elliptical polarisation state after reflection [20]. To understand ellipsometric measurement, the reflection of a light wave on a surface is considered below.

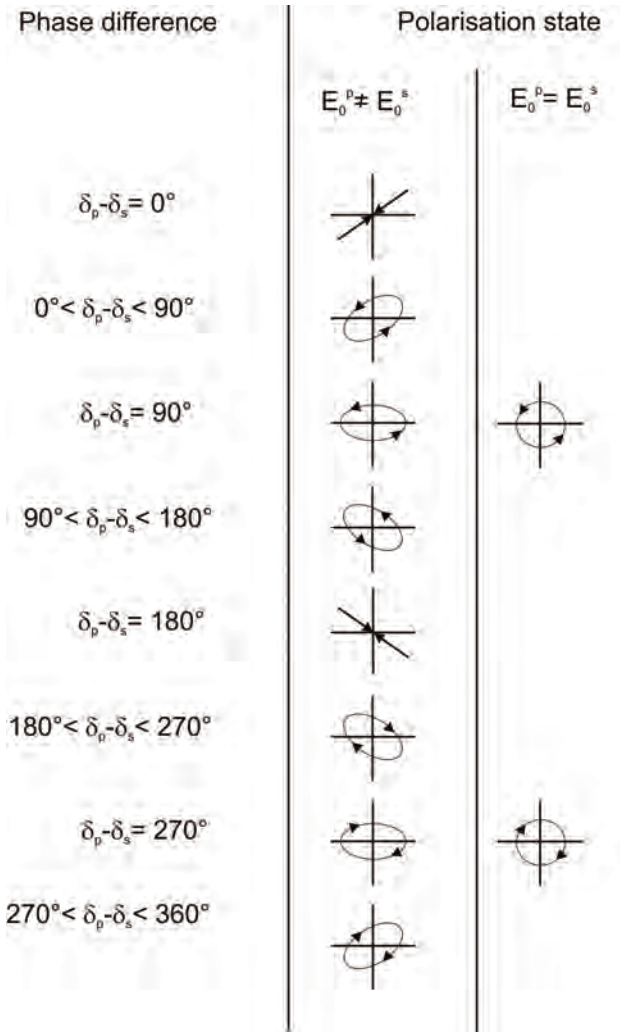

Figure 2.1: Resulting states of polarisation from superposition of E_0^p and E_0^s

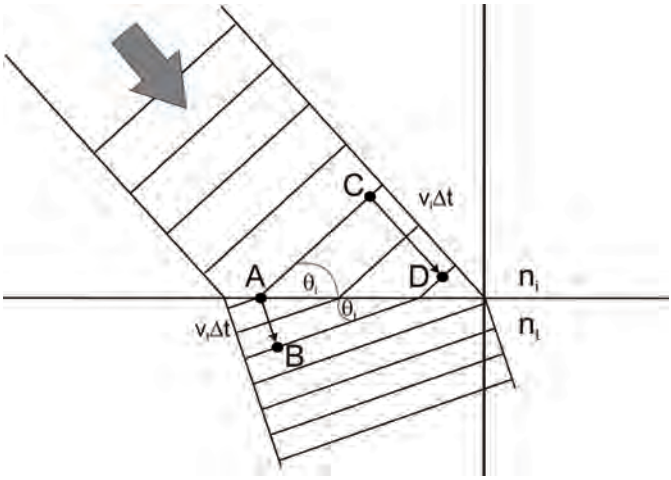

Figure 2.2: Wave front refracted at an interface

Snell's Law When a light beam hits an interface between two transparent media, the wave is refracted (partly transmitted and partly reflected), as the velocity and thus the propagation direction changes at the interface. The direction of refraction can be calculated using Snell's Law. In Figure 2.2 a wave front refracted at an interface between two media, with refractive index n_i (incident medium) and n_t (transmitted medium) respectively is shown.

The time to travel from C to D in the incident medium is the same as to travel from A to B in the refracting medium. It is

$$\frac{\sin\theta_i}{\overline{CD}} = \frac{\sin\theta_t}{\overline{AB}} \tag{2.12}$$

and with $\overline{CD} = v_i \Delta t$ and $\overline{AB} = v_t \Delta t$ it is

$$\frac{\sin\theta_i}{v_i} = \frac{\sin\theta_t}{v_t}. \tag{2.13}$$

Using the definition of the index of refraction (Equation 2.4) Snell's Law is obtained:

$$n_i \sin\theta_i = n_t \sin\theta_t \tag{2.14}$$

If the light beam travels from an optically less dense medium to an optically more dense medium, i.e. $n_i < n_t$ then is $\theta_i > \theta_t$ and the light beam is refracted towards the normal. Vice versa if $n_i > n_t$ the light beam is refracted away from the normal (see Figure 2.2) [21].

When considering an absorbing material the complex index of refraction has to be used and Snell's Law is defined as [20]

$$N_i \sin\theta_i = N_t \sin\theta_t. \tag{2.15}$$

Fresnel equations An incident (i) light beam is reflected (r) and transmitted (t) partly at an interface between two transparent homogenous media. Two cases can be distinguished: p-polarised state when the electric field is parallel to the plane of incidence and s-polarised state when the electric field is perpendicular to the plane of incidence. In Figure 2.3 the two cases with corresponding electric and magnetic field vectors are schematically illustrated [20, 21].

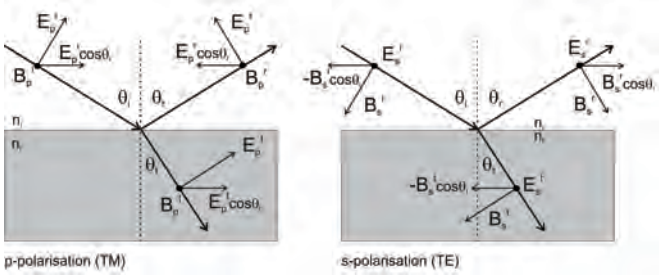

Figure 2.3: Electric and magnetic field vectors of p- and s-polarised incident (i) light, which is reflected (r) and transmitted (t) at an interface

Electric and magnetic fields are described using Maxwell's equations, which form the basic of the theory of electromagnetic waves [23]. Consequences of Maxwell's equations are used here, but mathematical derivations are omitted at this point. In case of a s-polarised wave, the electric and magnetic field components, which are tangential to the interface, have to be continuous due to the required boundary conditions for electromagnetic waves in Maxwell's equations:

$$\begin{aligned} E_s^t &= E_s^i + E_s^r \\ -B_s^t/\mu_t \cos\theta_t &= -B_s^i/\mu_i \cos\theta_i + B_s^r/\mu_r \cos\theta_r. \end{aligned} \tag{2.16}$$

With the magnetic induction B and μ the magnetic permeability. The letters i, r, t declare incident, reflected and transmitted part respectively. Since the most used materials in practice are dielectrics and thus $\mu_r = \mu_i = \mu_t = \mu_0$ (μ_0 is the permeability in vacuum) the equation 2.16 can be written as

$$-B_s^t \cos\theta_t = -B_s^i \cos\theta_i + B_s^r \cos\theta_r. \tag{2.17}$$

Furthermore, since $B_i = E_i/v_i$, $B_r = E_r/v_r$ and $B_t = E_t/v_t$ and with $v_i = v_r$ and $\theta_i = \theta_r$, Equation 2.17 can be written as

$$((E_s^i - E_s^r)\cos\theta_i)/v_i = (E_s^t \cos\theta_t)/v_t \tag{2.18}$$

With the definition of the refractive index (Equation 2.4)

$$n_i(E_s^i - E_s^r)\cos\theta_i = n_t E_s^t \cos\theta_t \tag{2.19}$$

is received. By eliminating E_s^t and using equation 2.16 the ratio of the reflected and incident electric field called the amplitude reflection coefficient r_s for s-polarised light is:

$$r_s = \frac{E_s^r}{E_s^i} = \frac{n_i \cos\theta_i - n_t \cos\theta_t}{n_i \cos\theta_i + n_t \cos\theta_t}. \tag{2.20}$$

In the same way the amplitude transmission coefficient can be derived:

$$t_s = \frac{E_s^t}{E_s^i} = \frac{2n_i \cos\theta_i}{n_i \cos\theta_i + n_t \cos\theta_t}. \tag{2.21}$$

In case of p-polarised light, the boundary conditions for electromagnetic waves in Maxwell's equations demand that

$$\begin{aligned} E_p^t \cos\theta_t &= E_p^i \cos\theta_i - E_p^r \cos\theta_r \\ B_p^i + B_p^r &= B_p^t. \end{aligned} \tag{2.22}$$

Equal to the derivation above, the amplitude transmission and reflection coefficient for a p-polarised wave can be obtained [21]:

$$r_p = \frac{E_p^r}{E_p^i} = \frac{n_t \cos\theta_i - n_i \cos\theta_t}{n_t \cos\theta_i + n_i \cos\theta_t} \tag{2.23}$$

and

$$t_p = \frac{E_p^t}{E_p^i} = \frac{2n_i \cos\theta_i}{n_t \cos\theta_i + n_i \cos\theta_t}. \tag{2.24}$$

In case of light absorbing media the index of refraction n must be replaced by the complex index of refraction N (Equation 2.5). In order to avoid complex angles Snell's law (Equation 2.15) is used. With $N_i^2 \sin^2\theta_i = N_t^2 \sin^2\theta_t$ and $\sin^2\theta + \cos^2\theta = 1$ the relation $N_t \cos\theta_t = (N_t^2 - N_i^2 \sin^2\theta_i)^{1/2}$ is obtained and the complex Fresnel equations are:

$$r_p = \frac{N_t/N_i \cos\theta_i - ((N_t/N_i)^2 - \sin^2\theta_i)^{1/2}}{N_t/N_i \cos\theta_i + ((N_t/N_i)^2 - \sin^2\theta_i)^{1/2}} \tag{2.25}$$

and

$$r_s = \frac{\cos\theta_i - ((N_t/N_i)^2 - \sin^2\theta_i)^{1/2}}{\cos\theta_i + ((N_t/N_i)^2 - \sin^2\theta_i)^{1/2}}. \tag{2.26}$$

Since

$$\begin{aligned} r_p &= |r_p|\, e^{i\delta_p} \\ r_s &= |r_s|\, e^{i\delta_s} \end{aligned} \tag{2.27}$$

the coefficients can be written as:

$$r_p = \frac{\left|E_p^r\right|}{\left|E_p^i\right|} e^{i(\delta_p^r - \delta_p^i)} \tag{2.28}$$

and

$$r_s = \frac{|E_s^r|}{|E_s^i|} e^{i(\delta_s^r - \delta_s^i)}. \tag{2.29}$$

The Fresnel equations are essential for ellipsometric measurements, since they are connected with the ellipsometric parameters.

2.2.3 Determination of ellipsometric parameters Ψ and Δ

In ellipsometric measurements the ellipsometric parameters Ψ and Δ are determined. Δ is the phase difference between p- and s-polarised wave upon reflection on the sample

$$\Delta = (\delta_p^r - \delta_s^r) \tag{2.30}$$

and $\tan\Psi$ is the ratio of the amplitude reflection coefficients $|r_p|$ and $|r_s|$ or the amplitude difference of p- and s-polarised wave after reflection on the sample, respectively:

$$\tan\Psi = \frac{|r_p|}{|r_s|} = \frac{|E_p^r|/|E_p^i|}{|E_s^r|/|E_s^i|} \tag{2.31}$$

With the definitions of the ellipsometric angles the basic equation of ellipsometry can be deduced:

$$\rho = \frac{r_p}{r_s} = \tan\Psi e^{(i\Delta)} = \frac{\left(\frac{E_p^r}{E_p^i}\right)}{\left(\frac{E_s^r}{E_s^i}\right)}. \tag{2.32}$$

With this basic equation of ellipsometry the optical constants (index of refraction and extinction coefficient) can be estimated by means of the Fresnel equations. Therefore, the ellipsometric angles Ψ and Δ must be determined. They are linked with the rotation angles of the optical elements (see Section 2.2.4) of an ellipsometer over a mathematical description of the polarisation state: Jones and Stokes formalism respectively are widely used methods to determine the effect of optical elements on the final polarisation state of a wave and to calculate the ellipsometric parameters [20].

Jones formalism Every state of polarisation can be expressed by superimposing two linear polarised plane waves as shown by Equation 2.11, which can also be written as matrix:

$$\vec{E}(\vec{r},t) = \begin{bmatrix} \vec{E}_0^p \cos(\omega t - \vec{k}\cdot\vec{r} + \delta_p) \\ \vec{E}_0^s \cos(\omega t - \vec{k}\cdot\vec{r} + \delta_s) \end{bmatrix} \tag{2.33}$$

and

$$\vec{E}(\vec{r},t) = \begin{bmatrix} \vec{E}_0^p e^{i(\omega t - \vec{k}\cdot\vec{r} + \delta_p)} \\ \vec{E}_0^s e^{i(\omega t - \vec{k}\cdot\vec{r} + \delta_s)} \end{bmatrix}, \tag{2.34}$$

respectively. Since the time dependence is not important in optical measurements, and the focus is on the ratio of amplitudes, the above equation can be abbreviated:

$$\vec{E}_J = \begin{bmatrix} \vec{E}_0^p e^{i\delta_p} \\ \vec{E}_0^s e^{i\delta_s} \end{bmatrix}. \tag{2.35}$$

This expression is the Jones vector which is a complex vector where the information about time and space of the wave is suppressed, but the complete information about polarisation is given in amplitudes and phases. E_p and E_s can assume any values and thus all possible polarisation states can be expressed [22]. The electric fields correspond to the light intensity which is expressed by:

$$I = I_p + I_s = |E_p|^2 + |E_s|^2 = E_p E_p^* + E_s E_s^*, \tag{2.36}$$

where E* is the complex conjugate of E. The light intensity is usually normalised ($I = 1$) and the Jones vector of linear polarised light parallel to p and s direction and at 45° respectively can be expressed by:

$$\vec{E}_{linear,p} = \begin{bmatrix} 1 \\ 0 \end{bmatrix} \quad \vec{E}_{linear,s} = \begin{bmatrix} 0 \\ 1 \end{bmatrix} \quad \vec{E}_{+45^\circ} = \frac{1}{\sqrt{2}} \begin{bmatrix} 1 \\ 1 \end{bmatrix} \tag{2.37}$$

Furthermore, the Jones vectors of right or left circularly, and elliptically polarised light are for example:

$$\vec{E}_R = \frac{1}{\sqrt{2}} \begin{bmatrix} 1 \\ i \end{bmatrix} \quad \vec{E}_L = \frac{1}{\sqrt{2}} \begin{bmatrix} 1 \\ -i \end{bmatrix} \quad \vec{E}_{elli} = \frac{1}{\sqrt{2}} \begin{bmatrix} 1/\sqrt{2} + i1/\sqrt{2} \\ i \end{bmatrix} \tag{2.38}$$

To describe the polarisation state of any electromagnetic wave after passing one or more optical devices (for details see Section 2.2.4) the Jones vector must be transformed by the Jones matrix, which represents the rotation of the optical devices or the assumed coordinate system, respectively. The matrices for the optical devices here presented are summerized in Table 2.1 [20].

Table 2.1: Jones matrices of optical devices

Optical device	Jones matrix
Polariser(P),Analyser(A) horizontal position	$\begin{bmatrix} 1 & 0 \\ 0 & 0 \end{bmatrix}$
P,A vertical position	$\begin{bmatrix} 0 & 0 \\ 0 & 1 \end{bmatrix}$
P,A $+45^\circ$ position	$1/2 \begin{bmatrix} 1 & 1 \\ 1 & 1 \end{bmatrix}$
Compensator	$\begin{bmatrix} 1 & 0 \\ 0 & e^{-i\delta} \end{bmatrix}$
Sample	$\begin{bmatrix} \sin\Psi e^{i\Delta} & 0 \\ 0 & \cos\Psi \end{bmatrix}$
Coordinate roation	$\begin{bmatrix} \cos\alpha & \sin\alpha \\ -\sin\alpha & \cos\alpha \end{bmatrix}$

Stokes formalism By means of the Stokes vector S, which is composed of the Stokes parameters, all states of polarisation can be determined by light intensity and electric fields respectively. The difference to the Jones formalism is that the description includes not only polarised, but also partly unpolarised or completely unpolarised light. The parameters are based on the light intensity and given in a xy-coordinate system by [22]:

$$
\begin{aligned}
S_0 &= I_x + I_y = E_{x0}^2 + E_{y0}^2 \\
S_1 &= I_x - I_y = E_{x0}^2 - E_{y0}^2 \\
S_2 &= I_{+45^\circ} - I_{-45^\circ} = 2E_{x0}E_{y0}\cos\Delta \\
S_3 &= I_R - I_L = -2E_{x0}E_{y0}\sin\Delta
\end{aligned} \tag{2.39}
$$

S_0 is the total light intensity and S_1 indicates a horizontal polarisation state ($S_1 > 0$) or a vertical polarisation state ($S_1 < 0$). From S_2 the polarisation state towards $+45^\circ$ ($S_2 > 0$) or towards -45° ($S_2 < 0$) is specified and S_3 describes the direction of rotation: right if $S_3 > 0$ and left if $S_3 < 0$. The correlation between the parameters is given by [22]:

$$
S_0^2 = S_1^2 + S_2^2 + S_3^2, \tag{2.40}
$$

and the degree of polarisation Π can be determined by:

$$
\Pi = \frac{\sqrt{S_1^2 + S_2^2 + S_3^2}}{S_0}. \tag{2.41}
$$

As in the Jones formalism the resulting Stokes vector must be transformed by a matrix and the resulting vector S_e describes the polarisation state of the light after passing the optical devices [20]:

$$
S_e = M \cdot S \tag{2.42}
$$

The accordant matrix called Mueller matrix M has the dimension 4x4 and is not necessary to this study.

2.2.4 Instrumentation

Composition of an ellipsometer

Ellipsometers usually consist of a light source (a laser beam with a specific wavelength or a lamp to vary the wavelength) radiating on the sample and a detector receiving the reflected light (see Figure 2.4). The angle of incidence (AOI) can be set. The optical devices of an ellipsometer and the sample can be arranged in different order. Depending on this arrangement, three or four Stokes parameters can be measured. A polariser is placed behind the light source, and an analyser in front of the detector. A compensator can be optionally placed on the light source or the detector side. Null ellipsometry has to be mentioned at this point as the first exercised type of ellipsometry. Null ellipsometry can be carried out using the human eye as a detector and was first used at the end of the 19th century. The principle is to rotate polariser and analyser so that the minimal light intensity is detected and the ellipsometric angles are determined from the rotation angles [24]. Polariser, analyser and compensator are described below.

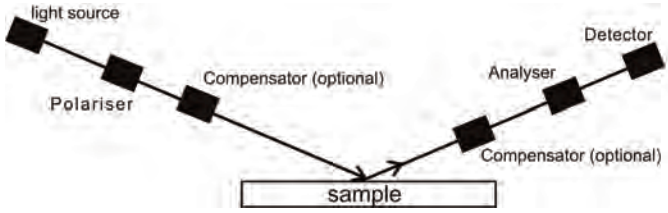

Figure 2.4: Schematically set-up of an ellipsometer

Polariser The polariser is arranged directly behind the light source to gain polarised from unpolarised light. It can be fixed or rotating. There are several options to polarise light: using birefringence, reflection or dichroism. Materials like quartz or calcite show birefringence which means anisotropy in the permittivity, thus in phase velocity and in the index of refraction. The orthogonal polarised parts of a light beam travel on different ways through the material, one named ordinary, the other extraordinary. To gain the desired polarisation

state, e.g. Nicol, Glan-Thompson or Rochon prisms are used. They consist of a birefringent crystal split diagonally and glued again. The ordinary ray is reflected at the interface crystal-glue, the extraordinary ray leaves the prism.

Polarisation by reflection is performed at a certain angle of incidence, called the Brewster's angle. Only the s-polarised part of a light beam is reflected on a glass plate, the p-polarised part is transmitted. Repeating this on several glass plates increases the degree of polarisation.

In dichroic materials e.g. in crystals like tourmaline, the absorption of the electromagnetic wave is dependent on the polarisation state. This effect is now widely used in polarisation foils made of cellulose with embedded iodine-quinine needles and can be produced cost-effectively [25].

Analyser The analyser is technically the same device as the polariser and can also be fixed or rotating. It is installed directly in front of the detector which determines the state of polarisation from the light intensity passing through.

Compensator The compensator is used to gain circularly polarised light from linear polarised light. Birefringent material (mostly magnesium flouride) is used. Dependent on the wavelength λ, index of refraction of ordinary (n_o) and extrordinary ray (n_e) and the thickness d of the crystal, a phase shift δ between s- and p- polarised electrical fields and thus a change in the polarisation state is enforced which is given by [21]:

$$\delta = \frac{2\pi}{\lambda} \left| n_o - n_e \right| d. \tag{2.43}$$

Modelling

The result of an ellipsometric measurement are the angles Ψ and Δ dependent on the wavelength and/or the angle of incidence. These angles refer to the dielectric function. To calculate the dielectric function, an adequate model has to be constructed, the dielectric function has to be modelled and the generated data have to be fitted to the measured progression of Ψ and Δ. Several models describing the dielectric polarisation and the resulting oscillation have been

developed. They are used according to requirements. An overview of the most important ones, the physical principles, and the application is given in Table 2.2.

Table 2.2: Overview of optical models to describe the dielectric function

Model	Basic theory	Material
Lorentz	electron oscillations in viscous fluid	general
Tauc–Lorentz	product of a unique bandgap + Lorentz	amorphous semiconductors; transparent conductive oxides
Drude	free electrons	metal semiconductor
Gauss	several Lorentz oscillators	general
Sellmeier Cauchy	$\epsilon_2 = 0$ in Lorentz	dielectric

2.3 Suface plasmon resonance enhanced ellipsometry (SPREE)

A special application of ellipsometry is the use of total internal reflection conditions combined with the surface plasmon resonance (SPR) effect. It is then called "Total internal reflection ellipsometry" (TIRE) or "Surface plasmon resonance enhanced ellipsometry" (SPREE) [7]. Typically, ellipsometry is used under external reflection conditions, i.e. the light beam travels from an optically lower dense medium (mostly air) to an optically denser medium (the sample) and is partly reflected and transmitted at the interface (see Figure 2.3).

In total internal reflection, the incident medium is optically denser than the transmission medium. Under this condition ($n_i > n_t$) and at a certain angle of incidence, called the critical angle of incidence $\theta_i = \theta_c$, no light is transmitted into the medium, but all incident energy is reflected and the refracted wave propagates along the interface. It is then $\theta_t = 90°$ and thus $\sin\theta_t = 1$ and Snell's Law (Equation 2.14) is $\sin\theta_c = n_t/n_i$. But when the angle of incidence becomes larger, the critical angle is $\theta_i > \theta_c$, consequently is $\sin\theta_t > 1$ and θ_t loses its physical sense. The Fresnel coefficents (Equations 2.20 and 2.23) must be considered under new conditions which are discussed below.

In a xyz coordinate system where x and y span the plane of incidence (x-direction is along the interface and y-direction is perpendicular to the interface), the wave vector (which is parallel to the propagation direction of the wave) of the transmitted wave is given by:

$$\vec{K_t}\vec{r} = K_{tx}x + K_{ty}y \tag{2.44}$$

with $K_{tx} = K_t \sin\theta_t$ and $K_{ty} = K_t \cos\theta_t$. The application of Snell's Law results in [26]:

$$\cos\theta_t = -i\left(\frac{\sin^2\theta_i}{(n_t/n_i)^2} - 1\right)^{1/2}. \tag{2.45}$$

With this expression the Fresnel coefficients for non-absorbing media, i.e. with real index of refraction can be written as [7]:

$$r_s = \frac{n_i\cos\theta_i + in_t\left[\frac{\sin^2\theta_i}{(n_t/n_i)^2} - 1\right]^{1/2}}{n_i\cos\theta_i - in_t\left[\frac{\sin^2\theta_i}{(n_t/n_i)^2} - 1\right]^{1/2}} \tag{2.46}$$

and

$$r_p = \frac{n_t \cos\theta_i + i n_i \left[\left(\frac{\sin^2\theta_i}{(n_t/n_i)^2}\right) - 1\right]^{1/2}}{n_t \cos\theta_i - i n_i \left[\left(\frac{\sin^2\theta_i}{(n_t/n_i)^2}\right) - 1\right]^{1/2}}. \tag{2.47}$$

The condition $|r_p| = \sqrt{r_p \cdot r_p^*} = \sqrt{r_s \cdot r_s^*} = 1$ is then given (r_s^* and r_p^* are the complex conjugates) and all energy is reflected, but no energy is transmitted into the medium. With the definition of the ellipsometric angle Ψ (equation 2.31) it is clear that $\Psi = 45°$. A difference in the reflected wave compared to the incident wave occurs only in the phase difference, which is the ellipsometric angle Δ (equation 2.30). By describing the reflection coefficients in complex numbers (equation 2.27) and using trigonometric functions, Δ is given by ([7]):

$$\begin{aligned}\Delta &= \delta_p - \delta_s \\ &= 2 \arctan \frac{\left(\sin^2\theta_i - \sin^2\theta_c\right)^{1/2}}{\tan\theta_i \sin\theta_i}.\end{aligned} \tag{2.48}$$

The progression of the ellipsometric angles Ψ and Δ over the angle of incidence can be simulated and are shown in Figure 2.5. Below the Brewster's angle (the maximum difference between r_s and r_p), Δ is 180°, above it is zero until the critical angle is reached. Above this value, Ψ is 45° as mentioned above and Δ is determined by Equation 2.48. Although the complete incident wave is reflected and thus there is no energy flow across the surface, the transmission coefficients (Equations 2.24, 2.21) are $t_{p,s} \neq 0$ when solving the equations. In fact, the energy flow is parallel but not normal to the interface and there is an evanescent field that penetrates into the medium. With the general equation for an electromagnetic wave (equation 2.8) and the definition for $\vec{K}$ given above (Equation 2.44), the transmitted wave is [21, 26]:

$$E_t = E_{0t} e^{-y\frac{2\pi}{\lambda}\left[(n_i \sin\theta_i)^2 - n_t^2\right]^{1/2}} e^{i\left(\omega t - x\frac{2\pi n_i}{\lambda}\sin\theta_i\right)} \tag{2.49}$$

with the wavelength in vacuum λ. This means the transmitted wave is propa-

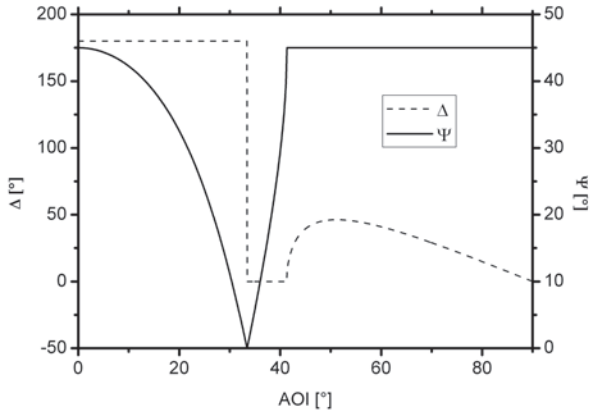

Figure 2.5: The ellipsometric parameters Ψ and Δ over the angle of incidence simulated for reflection on a glass/air interface under TIRE conditions, λ=632.8 nm

gating in x-direction (along the interface) with exponential decay and the amplitude penetrates perpendicular to the interface into the transmitted medium and decreases quickly (denoted as y-direction in Equation 2.49). How fast this evanscent field decreases is given by the first exponential term which is determined by the refraction indices and the angle of incidence. When calculating the penetration depth, values below 100 nm were found [7].

When expanding the two media system glass/air to a three media system glass/metal/air with the refractive indices N_g,N_m and N_a the resulting Fresnel equations are more complicated. The incident light beam is refracted at the interface glass/gold, partially reflected back into the glass and partially transmitted through the metal layer as the evanescent wave which gives rise to excitations at the interface metal/air [27]. These are collective longitudinal excitations of the conduction electrons in the metal, also called plasma oscillation. The resulting quasiparticle is called surface plasmon (SP) [28]. The resonance of these SPs oscillations at the metal surface are influenced by marginal changes in the physical properties like changes in the index of re-

fraction due to the adsorption of gas molecules and can be used for detecting (SPR effect).

The collective Fresnel coefficient for total internal reflection of p-polarised waves in such a system (glass/metal/air) is derived by summing up the partial waves which leads to an infinite series whereas the sum is given by [22]:

$$R_{gma} = \frac{r_{gm} + r_{ma}e^{-i2\beta}}{1 + r_{gm}r_{ma}e^{-i2\beta}} \tag{2.50}$$

with

$$\beta = K_m d_m = \frac{2\pi d_m}{\lambda} N_m \cos\theta_m \tag{2.51}$$

where d_m is the thickness of the metal layer. To determine the Fresnel coefficents as well as Ψ and Δ for total internal reflection combined with the excitation of SPs, the complex wave vector of a surface plasmon wave must be considered, which is given by:

$$K_{sp} = K'_{sp} + iK''_{sp} = \frac{2\pi}{\lambda}\sqrt{\frac{\epsilon_m\epsilon_a}{\epsilon_m + \epsilon_a}} = K'_{sp} + i\Gamma_i \tag{2.52}$$

where Γ_i represents the internal damping. This damping is due to the decay of electron-hole pairs excited by the electromagnetic field of the surface plasmon wave which produces heat. Since the metal layer must be thin enough to let light pass which can excite the SPs at the metal/air interface, a thin semitransparent metal layer is used and in addition a radiation damping Γ_{rad} plays a role. This phenomenon is attributed to the emitted radiation of the SP waves back into the glass. Therefore, the term $K^{rad}_{sp} + i\Gamma_{rad}$ must be added to the wavevector and

$$\begin{aligned} K_{sp} &= K'_{sp} + i\Gamma_i + K^{rad}_{sp} + i\Gamma_{rad} \\ &= K'_{sp} + K^{rad}_{sp} + i\left(\Gamma_i + \Gamma_{rad}\right) \end{aligned} \tag{2.53}$$

is received. It can be shown that only p-polarised (TM) waves can exist at the interface metal/air and s-polarised (TE) waves are mathematically impossible [26]. This means that only p-polarised waves are coupled into the metal and induce electron oscillation which leads to SP waves. Therefore, only the complex Fresnel coefficient for reflection of p-polarised waves is of interest. It was developed by Raether [27] to:

$$R_p = \left|r^p_{gm}\right| \frac{K_x - \left(K'_{sp} + K^{rad}_{sp}\right) - i\left(\Gamma_i - \Gamma_{rad}\right)}{K_x - \left(K'_{sp} + K^{rad}_{sp}\right) - i\left(\Gamma_i + \Gamma_{rad}\right)} \tag{2.54}$$

where $K_x = \frac{2\pi}{\lambda} N_g \sin\theta_g$

When no p-polarised light is reflected ($R_p = 0$), i.e. all incoming energy is coupled into the metal, the surface plasmon resonance effect and therefore the sensor sensitivity are at their maximum. This is given when $K_x = K'_{sp} + K^{rad}_{sp}$ (which is dependent on the angle of incidence θ_g and the wavelength) and $\Gamma_i = \Gamma_{rad}$. With the basic equation of ellipsometry (Equation 2.32) ρ is given by:

$$\rho = \frac{R_p}{R_s} = \frac{r^p_{gm} K_x - \left(K'_{sp} + K^{rad}_{sp}\right) - i\left(\Gamma_i - \Gamma_{rad}\right)}{R_s K_x - \left(K'_{sp} + K^{rad}_{sp}\right) - i\left(\Gamma_i + \Gamma_{rad}\right)} \tag{2.55}$$

and the ellipsometric angles Ψ and Δ by:

$$\tan\Psi = \frac{\left|r^p_{gm}\right|}{|R_s|} \sqrt{1 - \frac{4\Gamma_i\Gamma_{rad}}{Q^2 + \left[\Gamma_i + \Gamma_{rad}\right]^2}}$$

and

$$\Delta = \arg\frac{r^p_{gm}}{R_s} + \arctan\frac{2Q\Gamma_{rad}}{Q^2 + \left(\Gamma_i + \Gamma_{rad}\right)\left(\Gamma_i - \Gamma_{rad}\right)} \tag{2.56}$$

with $Q = K_x - \left(K'_{sp} + K^{rad}_{sp}\right)$. The situation $\Gamma_i = \Gamma_{rad}$ is desired since the in-

tensity of the electromagnetic field on the metal surface and thus the enhancement due to SPR is the highest [27]. But in a real measurement $\Gamma_i = \Gamma_{rad}$ is never satisfied due to non-idealities, there will be always a discrepancy $\delta\Gamma = \delta\Gamma_i - \delta\Gamma_{rad}$ and the ellipsometric angle Δ is given by [29]:

$$\Delta = \arg \frac{r_{gm}^p}{R_s} + \arctan \frac{1}{\frac{Q}{2\Gamma_i} + \frac{\delta\Gamma}{Q}}. \tag{2.57}$$

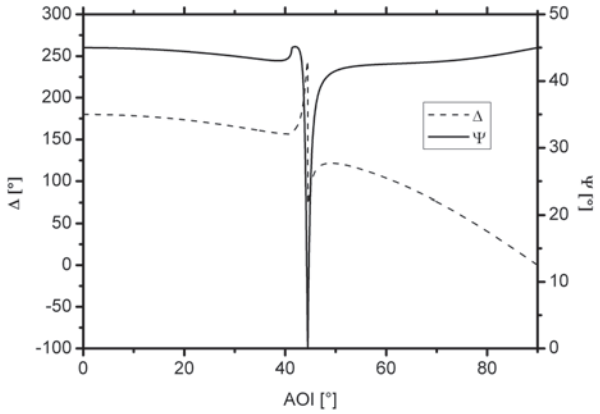

Figure 2.6: The ellipsometric parameters Ψ and Δ over the angle of incidence simulated for reflection on a glass/air interface with 45 nm gold as interlayer under TIRE conditions, λ=632.8 nm

Figure 2.6 shows the simulated progression of the ellipsometric parameters over the angle of incidence for a glass/metal/air system (the metal is 45 nm gold, λ = 632.8 nm) based on the Fresnel formalism. The progression of Ψ and Δ is now influenced by the SPR. At the SPR angle Ψ is close to zero, because the reflection coefficient R_p is close to zero since the maximum part of p-polarised light is coupled into the gold layer. Δ shows a large gradient around this angle and is therefore very sensitive to marginal changes in the system. Any change in the system, e.g. a modification of the refractive index,

leads to a different minimum SPR angle in Ψ and a shift of the gradient in Δ, respectively. The slope in Δ is steeper than in Ψ. Hence, sensing measurements have been performed in the region around the minimum SPR angle with Δ as the measured quantity.

3 Experimental details

In this work, surface plasmon resonance with ellispometric read-out was used for gas detection on thin sensitive layers. In this chapter, an overview of the instrumental set-up, the applied measuring methods, the production as well as the surface investigation of the layers and the investigated gases is presented.

3.1 Experimental Methods

3.1.1 Instrumental configuration

Measuring cell There are different geometrical set-ups using a prism and a thin metallic film to exploit the SPR effect. Established measuring set-ups include the Otto configuration with a thin air gap between prism and metallic layer and the Kretschmann-Raether configuration with the metallic layer placed directly on the prism [27, 30, 31]. In this work, the Kretschmann-Raether configuration was used (Figure 3.1). To investigate different layers and to change them easily, BK7 glass slides (25 x 25 x 1 mm^3) were coated with a gold layer and this one was top-coated with an additional layer. The prism was positioned on the glass slide with anisole as index matching liquid. The disadvantage of the combination prism/anisole/slide is the need to replace the index matching liquid as it evaporates within a few hours. After changing the anisole it is impossible to relocate the exact same measuring point. The optical set-up was placed on a self-made copper measuring cell acting as heat reservoir (see Figure 3.2). The analyte gases were dosed with a constant volume flow rate (set with the massflow controller MFC, multi gas controller 647B, MKS) through the measuring cell to get in touch with the sensitive layer in the measuring chamber. The utilised ellipsometer was a SE 400 from Sentech with

a Helium-Neon-Laser (wavelength 632.8 nm, input-polarisation: linear 45°), a polariser, a compensator and a rotating analyser with a manual goniometer (AOI spectrum from 40°to 90°, resolution 0.1°).

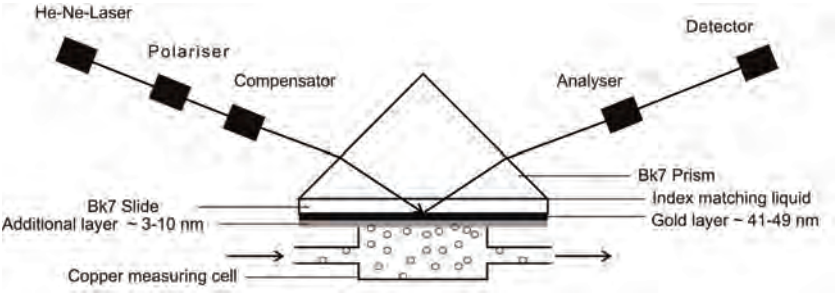

Figure 3.1: Schematic measuring set-up for ellipsometric monitoring of gases using the Kretschmann configuration

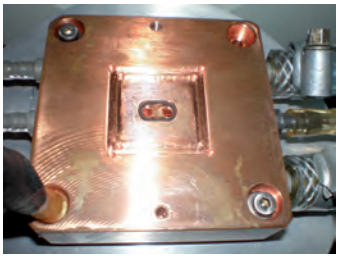

Figure 3.2: The copper measuring cell with the recesses for the slide and the prism, gas entrance and exit and the O-ring which delimits the measuring chamber

Pipe To investigate the sensor behaviour in a pipe line, a prism (BK7 glass, 7 mm x 10 mm) was coated directly with a Au/TiO_2 system and applied to a stainless steel tube (diameter 9 mm). The prism was placed on a filed opening and sealed with rubber. The set-up is shown schematically in Figure 3.3 and a photograph of this configuration is presented in Figure 3.4. The intention is to simulate a potential application in industry and to allow investigations concerning pressure and flow.

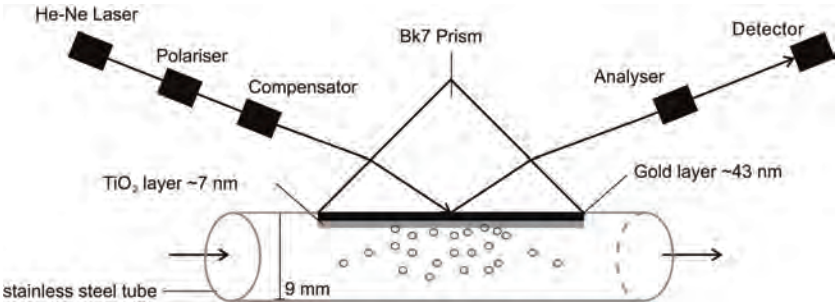

Figure 3.3: Schematic set-up of the Kretschmann configuration at a pipe

Figure 3.4: Image of a Au/TiO_2 coated prism installed on a pipe

3.1.2 Measuring methods

AOI dependent measurements

To locate the position of the SPR effect, the ellipsometric parameters Ψ and Δ were quantified over the angle of incidence. This measurement type was used to investigate the shift in position of the SPR effect in different gas atmospheres and the long-term stability of the sensitive layers (weeks or months). The analyte gases were dosed with a constant volume flow rate of 50-100 ml/min through the measuring cell and synthetic air or nitrogen were used as reference gas.

Fix AOI measurements

Time dependent measurements were performed by fixing an AOI at a sensitive point of the SPR effect determined by a previous AOI dependent measurement. Since the change in the Δ values is higher compared to Ψ due to the high slope, Δ was used as measuring signal and quantified over time. This measuring type was used to determine the lowest detectable concentrations of the analyte gases and to perform long-term measurements without interruption (hours in case of the measuring cell and up to months in case of the tube).

3.2 Deposition of layers

3.2.1 Gold layers

The gold layers were initially produced at Accurion GmbH, Germany. Later, they were produced at BAM in a coating plant (von Ardenne CS 730 ECS) with electron beam evaporation. Gold was evaporated from an Al_2O_3 cup with 7 kV accelerating voltage and $8 \cdot 10^{-6}$ mbar residual pressure. A gold layer of 40-49 nm thickness was deposited with a rate of 0.1 nm/s on a BK7 slide (25 x 25 x 1 mm^3) or a BK7 prism (base area 8 x 10 mm^2), which was cleaned before by an argon ion beam. An adhesive layer, a 2 nm thick layer of a nickel chrome composition was deposited between the substrate and the gold layer

(8 kV acceleration voltage, $5 \cdot 10^{-7}$ residual pressure, 0.05 nm/s deposition rate).

Cleaning of gold layers Before being used for experiments and before coating the layers with an additional layer, the gold coated BK7 substrates were cleaned chemically with the Radio Corporation of America (RCA) method. They were heated for 10 min in a 75℃ mixture of water, 25 % ammonia solution and 25 % hydrogen peroxide solution (volume ratio 5:1:1) [32]. Then the slides were rinsed with water and ethanol and dried in a nitrogen flow.

3.2.2 Top-coated gold layers

The gold layers were top-coated with thin layers of different inorganic materials.

Physical vapour deposition

TiO_2 layers were manufactured at BAM by physical vapour deposition (PVD) in a coating plant (von Ardenne CS 730 ECS) with electron beam evaporation. Granulate material of Ti_3O_5 was evaporated under oxygen deficiency conditions and substoichiometric TiO_2 deposited with 0.1 nm/s rate of growth.

Sol-gel process

The MgF_2, ZnO_2 and TiO_2 layers were produced by means of a sol-gel (SG) process and the spin-coating technique. ZrO_2 layers were produced at BAM and of a commercial ZrO_2 sol (ZRO2-ACT, NYACOL). The gold slides were wetted with a 0.5 % (w/w) sol and spin-coated at 5000 rounds per minute (rpm) for 40 s using a self-made spin coater. Finally, the layers were heated for 2.5 h at 120 ℃. The TiO_2 layers were produced at the Humboldt-Universität zu Berlin (HUB) with a 0.01 M ethanolic $Ti(O^iPr)_4$ sol with an equimolar amount of water and a catalytic amount of hydrochloric acid using a spin-coater KW-4a (Chemat Technology) at 5000 rpm for 40 s . The layers were heated for 2 h at 100 ℃ [33].

The MgF_2 layers were made at HUB with a MgF_2 sol consisting of a suspension of magnesium methoxid in methanole and a non-aqueous hydrogen fluoride solution in methanol (molar ratio 1:2) using a spin-coater KW-4a (Chemat Technology) at 5000 rounds per minute (rpm) for 40 s. The layers were heated for 2 h at 100 ℃ [34].

Magnetron sputtering

Iron doped tin oxide Fe : SnO_2 layers were deposited by magnetron sputtering at J.E. Purkinje University, Czech Republic. The radio frequency (RF) 13.56 MHz power supply Advance Energy Dressler Intergo 133 was used with high intensity NdFeB magnets and targets of 99.9 % SnO_2 (thickness 3 mm). The doping was achieved by placing iron strips (99.95 % iron, 10 x 20 x 2 mm^3) that overlapped partially the erosion zone. The deposition had taken place by argon ion bombardment at 20 W RF power at argon (99.9999 %, Linde) pressure of 0.8 Pa for 3 min.

3.3 Characterisation of layers

The gold layers as well as the thin additional layers deposited on gold were investigated using different measuring methods in order to characterise the surface structure.

3.3.1 Scanning electron microscopy (SEM)

The surface topology was studied by scanning electron microscopy (SEM) at BAM with a Zeiss Gemini Supra 40 microscope and with energy-dispersive X-ray (EDX) spectroscopy with a spectrometer type Thermo NSS 2.1, Bruker Quantax 400. The acceleration voltage was 5 or 10 kV respectively, magnitude was 20.000-200.000.

3.3.2 Atomic force microscopy (AFM)

The layer surfaces were investigated furthermore with atomic force microscopy (AFM) at BAM with an Atomic Force Microscope Dimension D 3100 (Digital Instruments/Veeco), with a lateral resolution of 1-10 nm and a height resolution of ca. 0.01 nm. The raw data were analyzed by the software WSxM 4.0 Develop 11.1.

3.3.3 Spectroscopic ellipsometry (SE)

Each deposited slide was investigated at BAM by spectroscopic ellipsometry (SE) mapping to determine the optical constants and thickness of the layer using a M2000DI ellipsometer (J. A. Woollam). The samples were measured at angles of incidence of 50°-75° (step 5°) in a spectral range between 190 nm and 1700 nm at 9 or 25 different measuring spots. The ellipsometric data were analysed using the WVASE32® software and performing the following steps:

- constructing a layer model, see Figure 3.5
- modelling the dielectric function of every single layer with optical models, see Table 2.2
- generate the dispersion of the ellipsometric parameters
- fitting the model to the experimental data

The fitting should result in a synchronization of the generated and the experimental data, which is achieved through regression analysis. The mean squared error (MSE) is used to quantify the distinction between curves. The unknown parameters (optical constants, thickness) are varied until the minimum MSE is reached. The lower the MSE, the better the accordance of generated and experimental data. The results of the WVASE32® software analysis are the dispersion of the optical constants and the thickness of the layers [35].

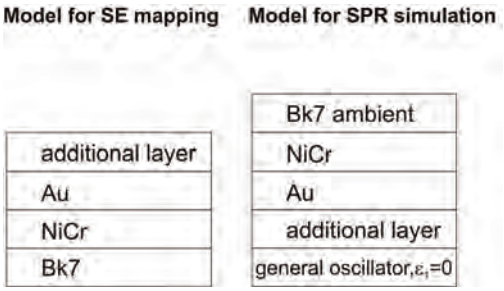

Figure 3.5: Layer systems as used for modelling in SE mapping and SPR simulation

Simulation of the SPR effect The WVASE32® software was also used to simulate the SPR effect of gold layers as well as of top-coated gold layers. Therefore, the layer model of the above described analysis was inverted and the top layer (BK7) set as ambient (see Figure 3.5). The progression of Ψ and Δ over angle of incidence at $\lambda = 632.8$ nm was generated to locate the position of the SPR effect and to determine the effect of the additional layers on the shape of the SPR curve.

3.3.4 Transmission electron microscopy (TEM)

One layer system (BK7/gold/TiO_2) was investigated by transmission electron microscopy (TEM) in order to understand the layer composition. This measurement was made at BAM with a transmission electron microscope type JEOL 4000FX with 400 kV acceleration voltage.

3.3.5 X-ray photoelectron spectroscopy (XPS)

The chemical surface composition was investigated by X-ray photoelectron spectroscopy (XPS) at J.E. Purkinje University, Czech Republic by using a XPS system with a base pressure below $3x10^{-7}$ Pa and a X-ray source, Al (1486 eV) at 12 kV and 200 W. The surface composition was calculated from the XPS spectra using the standard RSF from CasaXPS software 2.93, 1, 14.8, 10.8 for O 1s, C 1s, Sn 3d5/2 and Fe 2p3/2 dominant peaks, respectively [36].

3.4 Analyte gases

Nitrogen (5.0, air liquide) or compressed air (air liquide) were taken as reference and diluting gas respectively. The investigated pure gases are methane (2.5, air liquide), ethane (2.5, Messer), propane (3.5, air liquide), n-butane (3.5, air liquide), helium (5.0, air liquide), hydrogen (5.0, air liquide), carbon monoxide (3.7, Messer), carbon dioxide (4.5, air products), oxygen (4.5, air liquide), and 1,1,1,2-Tetraflouroethane (2.5 R134a, Hoechst). Furthermore, different test gases prepared at BAM were used: ammonia (8 % in air), hydrogen (0.25 % in nitrogen), methane (0.46% in air), propane (0.5 % in air), carbon dioxide (1.7 % in air), carbon monoxide (100 ppm in air). These test gases were also used to mix concentrations in the low ppm region.

3.5 Refractive index calculation

The refractive index of the investigated gases was calculated by the polarisability of the accordant gas molecule or atom respectively:

$$\epsilon = 1 + \frac{N_a p 4\pi\alpha}{R_g T} \tag{3.1}$$

with the dielectric constant ϵ, the Avogadro constant N_a, the polarisability α, the gas constant R_g, pressure p and temperature T. The calculated values for the refractive index of several gases are summarised in Table 3.1.

Table 3.1: Calculated refractive indices for different pure gases at 20 ℃

gas	calculated n
CH_4	1.00041
H_2	1.00013
CO_2	1.00046
N_2	1.00027
He	1.000032
O_2	1.00025
O_3	1.00050
C_3H_8	1.001

Part II

Results and Discussion

4 Gold layers

As shown in Chapter I, surface plasmon resonance (SPR) can be generated in metal layers and used in sensor applications. In this work, SPR in gold layers with ellipsometric read-out has been investigated concerning the detection of gases. Gold has been chosen due to its chemical stability [37]. It can be deposited in very thin layers e.g. by chemical vapour deposition [38] or hydrogen assisted reduction [39]. The gold layers were deposited on BK7 glass by physical vapour deposition with nickel-chrome as the adhesive layer at two different facilities (internal at BAM and extern by contract coating at Accurion GmbH, Göttingen, Germany). The topics of the following sections will include surface characterisation of the gold layers, the simulation of the SPR effect on gold and the results of gas sensing experiments using gold as a sensitive layer.

4.1 Surface analysis

To gain an impression of the surface quality the gold layers have been investigated by means of scanning electron microscopy (SEM) and atomic force microscopy (AFM). Spectroscopic ellipsometry (SE) mapping has been used to determine the optical constants and the thickness of the layers.

4.1.1 Scanning electron microscopy (SEM)

Figure 4.1 shows the result of a SEM measurement on the surface of a gold layer with a thickness of 45 nm produced externally. The surface has a regular microstructure with visible flat particles of the same size up to a diameter of 200 nm. The SEM measurements of the internally produced gold layers showed a similar regular structure with rounder particles (image not shown).

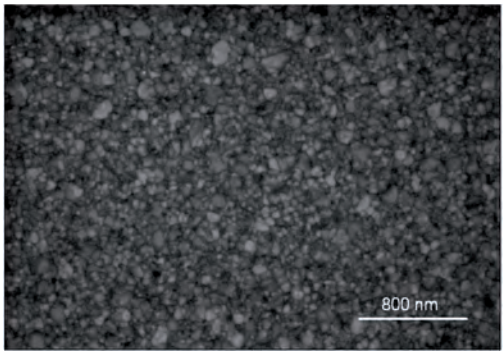

Figure 4.1: SEM image of a 45 nm gold layer deposited on BK7 glass. Magnitude: 100000, EHT: 10 kV

In literature, comparable gold surfaces were found: a 45 nm gold layer on silicon produced by PVD, which shows also a regular structure with round particles up to a diameter of 100 nm [40], and round particles with a crystal size of 40 - 60 nm of a gold film produced by hydrogen assisted reduction on nickel [39].

4.1.2 Atomic force microscopy (AFM)

The gold layers were measured by means of AFM, which shows similar results to the SEM measurements (see Figure 4.2). The surfaces are flat since the average surface roughness were determined by AFM analysis to R_a=1.3 nm for internally as well as for externally manufactured gold layers. Sputtered gold layers (45 nm thickness) reported in literature are also smooth and show a slight difference in surface roughness depending on the substrate: R_a=1.26 nm for gold sputtered on silicon and R_a=0.95 nm sputtered on aminopropyltrimethoxysilane (APS) [40].

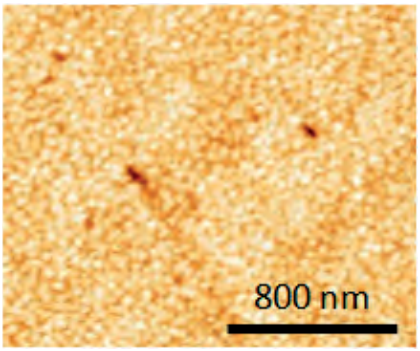

Figure 4.2: AFM image of a 45 nm gold layer deposited on BK7 glass

4.1.3 Spectroscopic ellipsometry (SE)

Every gold layer was investigated by SE to determine the optical constants and the thickness of the layer. Therefore, every layer was mapped: the dispersion of the ellipsometric parameters was quantified by SE on 9 different spot sizes. Exemplarily, the measured ellipsometric parameters in the center of a gold layer are shown in Figure 4.3 (solid lines). The experimental values were analysed by the software (see Section 3.3). A three layer system model was built (top to bottom):

Au layer (three Gauss and one Drude oscillators)
4.7 nm NiCr (three Lorentz oscillators)
BK7 [41]

The generated values are presented in Figure 4.3 as circles. The fitting procedure resulted in the optical constants presented in Figure 4.4. The refractive index has a maximum of 1.76 in the visible region. It decreases above 500 nm, whereas the absorption of the layer increases rapidly up to 12. At $\lambda = 632.8$ nm, which is the wavelength used in the gas sensing experiments, the values are n = 0.19 and k = 3.5. The optical constants are in good agreement with literature values, which are plotted as solid lines [42]. Also other sources present similar results for the dispersion of the optical constants [43, 44].

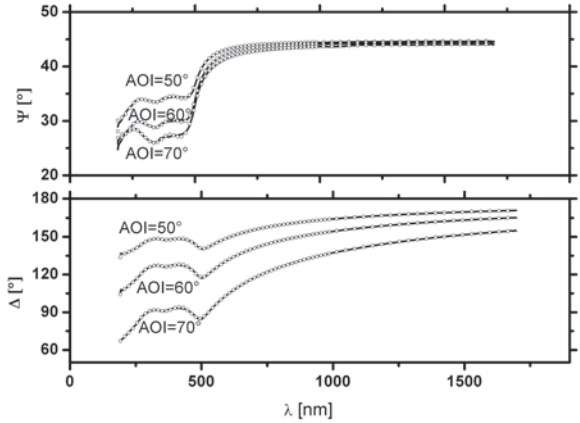

Figure 4.3: Dispersion of the ellipsometric angles Ψ and Δ of a 43 nm thick gold layer. Solid lines: experimental, circles: model

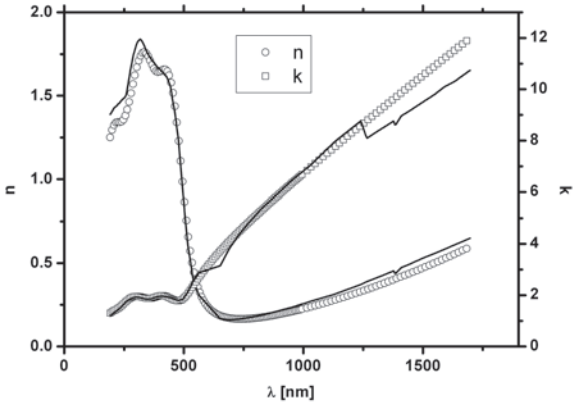

Figure 4.4: Dispersion of SE determined optical constants n and k of a gold layer deposited on BK7. Solid lines: literature values [42]

The optical constants were determined for one point in the centre of the layer and the results were used to quantify the thicknesses at all nine measuring spots. The determined thicknesses of the different measuring spots on the gold layer vary between 42.6 and 43.2 nm, whereas the fitting procedure resulted in final MSEs of 4.7 - 4.9. In order to visualise the differences in the surface thickness, the determined values are presented in Figure 4.5. The x- and y - axes demonstrate the measuring spot on the surface. Similar results were achieved for all other gold layers: The thickness of a single gold layer varies up to 2 nm. The range expands when comparing the gold layers to each other: gold layer thicknesses between 41 and 51 nm were determined. For all thicknesses of gold layers, the value of the centre of the layer is quoted in the following discussions.

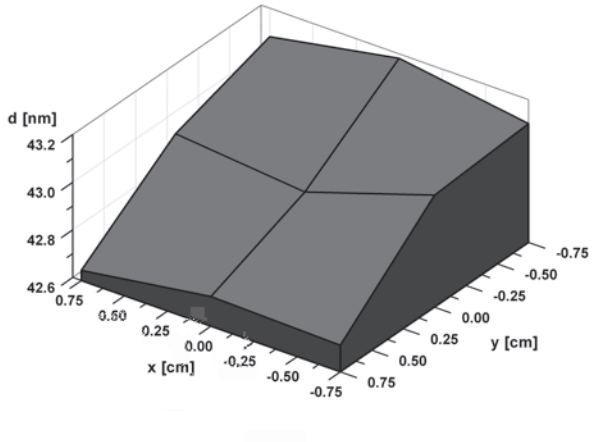

Figure 4.5: Thickness inhomogeneity of a 2.5 cm x 2.5 cm gold layer

4.2 Theoretical consideration of the SPR effect

The sensor system consists of a three layer system: glass/metal/gasatmosphere. The progression and the location of the AOI-spectra (SPR effect) are dependent on the optical properties of the materials and the wavelength of the incident light. The wavelength is defined as $\lambda = 632.8$ nm by the monochromatic He-Ne-laser of the SE400 ellipsometer, utilised for gas sensing experiments. The goniometer is limited to an AOI of 40° - 90°. Therefore, the glass should have an index of refraction which shifts the position of the SPR effect into this region. After simulating the resulting SPR effects with different glasses (results not shown), BK7 was chosen as suitable material. The following model was generated to simulate the SPR effect for a BK7/Au/vacuum system (top to bottom):

BK7 as ambient material [41]
NiCr (three Lorentz oscillators)
48 nm Au (three Gauss and one Lorentz oscillators)
vacuum/gas ($\epsilon_2 = 0$, $\epsilon_1 = 1 + x$)

In Figure 4.6, the results of the simulation are presented, the solid line depicts the SPR effect in vacuum. The thickness of the gold layer was varied until Ψ reached its minimum (2.8°). At this AOI (43.6°), most of the p-polarised part of the light is coupled into the metal. To simulate a gas atmosphere underneath the gold layer, ϵ_1 was changed to the accordant value of nitrogen and propane, calculated from the index of refraction (see table 3.1). With an increasing refractive index, the SPR curve is shifted to higher values of AOI. The difference in the third decimal place of the index of refraction between propane and nitrogen should cause a shift of the minimum AOI of at least 0.05° in practice.

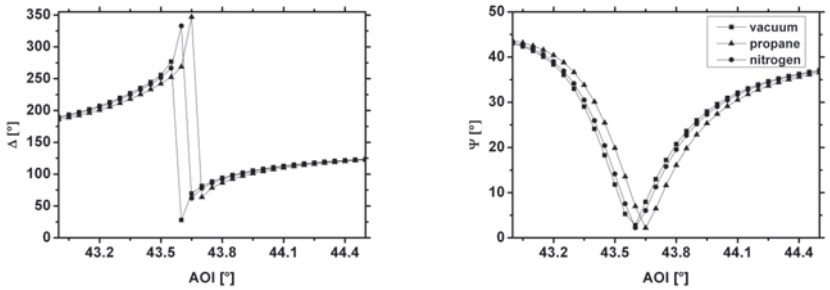

(a) Δ-AOI spectrum (b) Ψ-AOI spectrum

Figure 4.6: Simulation of the SPR effect in different gas atmospheres on a gold layer

4.3 Gas sensing

Sensing gases with the measuring arrangement presented here is based on refractive index changes. The processes which happen on the surface cannot be proven. However, theoretical assumptions were made and several mechanisms responsible for gas sensing are hypothesised (see Figure 4.7):

1. the **change in the index of refraction** in the analyte volume, no interaction between analyte gas and the sensor surface
2. the **formation of an adsorbed layer**
3. the **diffusion of the analyte gas** into the sensor layer
4. the **solvation of the analyte gas** in the sensor layer

The change in the refractive index of the analyte volume as reason for a response in Δ is the obvious mechanism. Depending on the type of gas there is an attraction between the sensor layer and the gas particles, an adsorbed layer is formed, the gas atmosphere is thus denser close to the surface and the refractive index increases. The diffusion of the gas into the layer is primarily possible with small gas particles like those in helium. By penetrating the

sensor layer, its optical constants are modified. In the case of solvation, the penetration of the layer results in a homogenous mixture of the gaseous and solid phases. The gas is completely dissolved in the gold. The mechanisms are assumed to occur simultaneously and this assumption is affirmed in part by the experiments presented in the next sections.

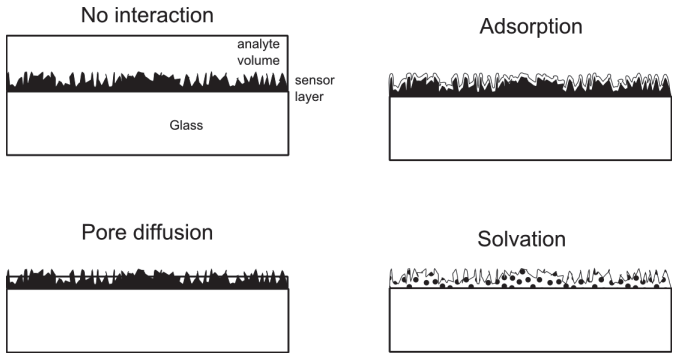

Figure 4.7: Schematical illustration of the supposed mechanisms responsible for gas sensing

In the following section, the SPR effect determined experimentally on gold in different gas atmospheres and the results of measurements with fixed AOI are presented.

4.3.1 AOI dependent measurements

By experimentally quantifying the ellipsometric angles Ψ and Δ over the angle of incidence (AOI), the position of the SPR effect can be located. But in this context, the results of the SE surface analysis have to be considered: the thickness of the gold surface is not homogenous and the marginal irregularities influence the laser spot of the here employed SE400 ellipsometer (diameter $\sim$2 mm). Therefore, the values for Ψ and Δ will vary by some degrees depending on the measuring spot on the layer. Based on the simulation in section 4.2, the SPR minimum in nitrogen atmosphere was expected to be 43.6°, but a small shift in the location of the SPR effect and a difference in

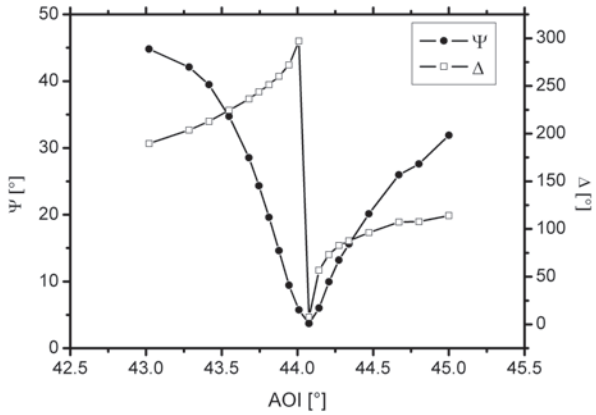

Figure 4.8: Experimentally determined SPR effect for one measuring spot on a 44 nm gold layer.

the Ψ minimum is expected. Measurements confirmed this effect: the shift of the AOI was determined up to 0.1° and the difference in the minimum up to 3°, depending on the measuring spot (results not shown). The SPR effect determined experimentally for one measuring spot of a 44 nm thick gold layer is shown in Figure 4.8, where the SPR minimum was found at an AOI of 44.08°. The measurement was performed without any volume flow rate of an analyte gas, i.e. in a laboratory atmosphere. The shapes of the Ψ and Δ curves are in good agreement with the simulation (compare Figure 4.6).

Due to the results of the simulation (see section 4.2), a shift in the position of the SPR effect is expected when changing the gas atmosphere and repeating the experiment. Indeed, this shift is larger than in the simulation as presented in Figure 4.9. The difference in the SPR minimum between nitrogen and propane atmosphere is 0.1°, whereas the simulation resulted in a shift of only 0.05°. In the simulation, only the change in the index of refraction of the gas atmosphere is considered. In practice, not only the change of the refractive index in the gas phase, but also the adsorption of the gas molecules on the gold surface can contribute to an influence on the surface plasmon oscillations

and on Δ, respectively. Adsorbed gas molecules slightly change the surface quality and therefore the optical properties. As can be seen in Figure 4.9 that the SPR effect is shifted to higher or lower AOIs, depending on the gas species and on the index of refraction respectively (see Table 3.1). Therefore a helium atmosphere causes a small shift to lower AOI compared to nitrogen. After exposing the sensor to propane and helium respectively, the experiment was repeated with nitrogen and the complete reversibility of the shift was observed.

The AOI dependent measurements show that pure gases can be distinguished by their index of refraction when using a reference gas and that the measurement strongly depends on the measuring spot.

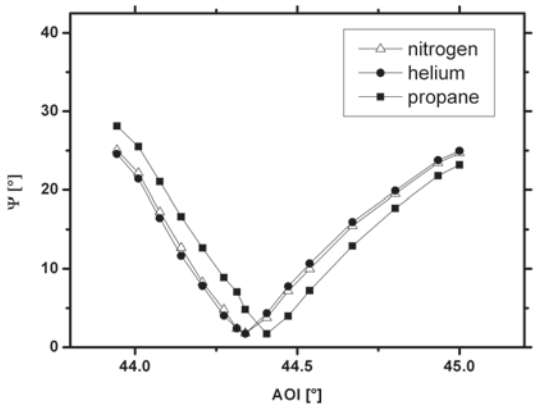

Figure 4.9: SPR effect on a 44 nm gold layer in different gas atmospheres

4.3.2 Fixed AOI measurements with non-polar gases

To perform measurements in order to detect changes in the gas atmosphere quickly, an obvious solution would be to fix the AOI and to use the ellipsometric parameters Δ or Ψ as a measured quantity. The large derivation in the phase Δ in AOI dependent spectra indicates a higher sensitivity to changes compared to the amplitude ratio Ψ. The higher sensitivity of the phase compared to the amplitude characteristics is also reported in literature [19] and thus, the phase

Δ was chosen as signal. The result of a measurement with fixed AOI on a 43 nm gold layer is shown in Figure 4.10. Several pure gases were dosed to the measuring cell alternately. The resulting graph provides several results. The correlation between Δ and the index of refraction (see Table 3.1) is even more obvious than in the AOI dependent measurement: assuming nitrogen as the reference gas, the gases with a higher refractive index cause a shift in Δ to higher values and vice versa. The difference in the refractive indices is in the fourth or fifth decimal place. For example, in case of nitrogen ($n_{632.8}$=1.00027) and oxygen ($n_{632.8}$=1.00025) the difference is $\Delta n = 2 \cdot 10^{-5}$ refractive index unit (RIU), and this causes a significant difference in the Δ values of 0.6°. Another important result of this measurement is the abrupt change in Δ, ending in a plateau. This fact indicates that the change of the refractive index of the gas atmosphere underneath the gold layer is more important than the formation of an adsorption layer. The atmosphere under the gold layer is stable as long as one gas flows at a constant rate. When switching to another gas, this one displaces the prior analyte and changes the atmosphere quickly. The formation of an adsorption layer would take longer. Furthermore, the measurement presented in Figure 4.10 shows the reversibility of the sensor system using the example of nitrogen. The second nitrogen plateau lies within the values of the first plateau even if other gases were present in the meantime. A small drift in the Δ values, present in the whole measurement independent on the gas type, can be observed. For example, the final value for nitrogen is 0.3° higher than the initial value. This drift was noticed in all fixed AOI measurements on gold layers, the probable cause is discussed in Section 4.5.

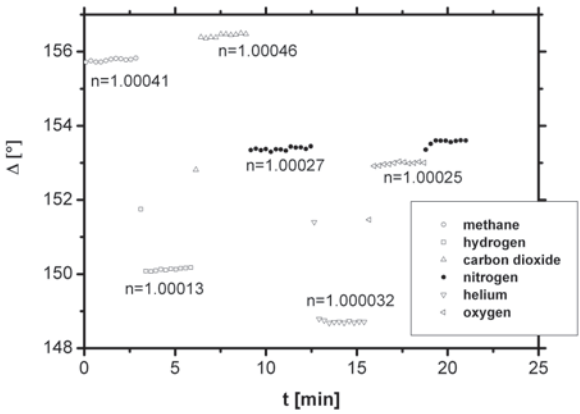

Figure 4.10: Dependency of phase Δ on the refractive index of pure gases with a constant volume rate flow of 100 ml/min. Data removed for clarity

4.3.3 Fixed AOI measurements with polar gases

Several gases were tested on gold and a difference between polar and non-polar gases concerning the progress in the Δ values was observed. In Figure 4.11, the exposure of the sensor to ozone (0.5 % (v/v) in oxygen) and oxygen (100 % (v/v)) is shown with nitrogen (100 % (v/v)) as reference gas. When switching from nitrogen to oxygen, the values decrease suddenly as expected due to the lower index of refraction of oxygen (see table 3.1). When switching to ozone (0.5 % (v/v) in oxygen), a slight increase of Δ is expected due to the higher refractive index of the diluted ozone compared to oxygen. Two facts can be stated: the response of Δ is large (45°) and the values change slower, asymptotically approximating a plateau. Hence, the formation of an adsorption layer is assumed. Adsorption means, the gas particles are attracted by surface forces and condense at the metal surface. If the forces are strong enough to bind the molecules/atoms long enough before evaporating again, the formation of a monomolecular/monoatomic layer that covers the surface is possible [45]. The accordant forces between the ozone molecules and the gold layer are obviously

due to the polarity of the gas. The large resonance of Δ is therefore not only caused by the change of the index of refraction in the gas atmosphere, but also by the densification of the gas atmosphere next to the gold surface due to the formation of an adsorption layer. After switching from ozone to oxygen a decrease in Δ is expected, but obviously the evaporation and desorption of the ozone molecules takes more time and happens only when purging with nitrogen.

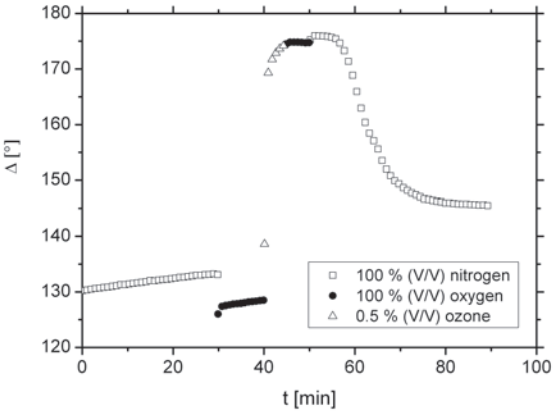

Figure 4.11: Detection of nitrogen, oxygen and ozone on a 43 nm gold layer. Data removed for clarity

The same phenomenon was observed in experiments with the polar gases ammonia and 1,1,1,2-Tetrafluoroethane (results not shown). No sudden change of the Δ values is visible here either, but a slow approximation to a plateau when switching to ammonia and reswitching to air respectively.

4.4 Detection limits

In the prior section the effect of pure gases on the ellipsometric angle Δ has been demonstrated. The next step is to dilute the gases to get lower concentrations. In Figure 4.12 the detection of diluted methane is shown. Nitrogen was

used as reference and dilution gas respectively and pure methane was diluted to 20, 40, 60 and 80 % (v/v). The reference gas passed through the measuring cell with 100 ml/min and methane was mixed additionally in 20 % steps every two minutes until 100 % methane was reached. The different concentrations cause clearly visible steps in the Δ values until the final value of the maximum concentration. Besides the dependence of Δ on the gas concentration, also two important properties of the sensor are shown in this graphic. The first is the response time t_{90}, i.e. the time the signal needs to reach 90 % of the final value [8]. It is obvious, that this time is required to be as small as possible for sensor applications. In the results presented here, the signal reaches the t_{90} level within one measurement interval, 5.5 s in this case. This is at least half the size of other reported values for t_{90} in literature (oxygen or ozone sensing by resistance measurement) [8, 9]. The t_{90} value for a typical semiconductor SnO_2 sensors is $\sim$ 10 s [10]. The second aspect is the statistical consideration of the measurement concerning the decision limit. The norm DIN 32645 declares the determination of a decision limit or detection limit respectively with a calibration function [46]. The calibration function has to be determined by calibration samples with defined analyte concentrations in order to calculate the decision limit of an analyte sample. In this case, the measurement presented in Figure 4.12 would serve to determine the calibration curve and be the analyte sample at the same time. Furthermore, it would be necessary to determine a calibration curve for every new measurement since the results differ due to the surface inhomogeneity. Nevertheless, detection limits were determined according to the norm. The distinction of the Δ response to the basic noise was considered. The average value in the plateau of the base line (nitrogen) and the first dilution steps are marked in Figure 4.12 as solid lines. The difference between the average value of the baseline and the first dilution step is 10 times that of the standard deviation σ of the basic noise, which gives much space for plateaus of concentrations below 20 % (v/v). Consequently, the gas has been diluted to lower concentrations until the Δ signal could not be distinguished from the basic noise (not shown). Generally, the concentration which causes a response that is three σ above or below the base line, is stated as the lowest detectable concentration (LDC) in this work.

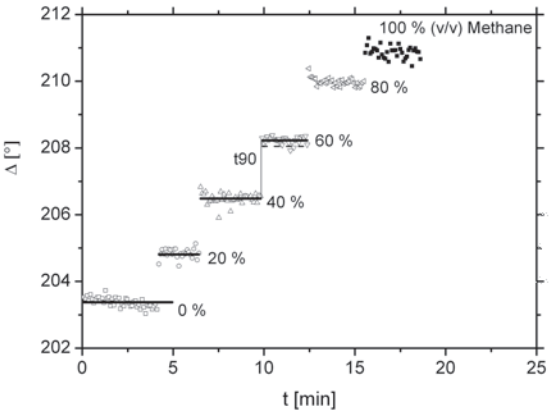

Figure 4.12: Detection of different methane concentrations on a 42 nm gold layer. Solid lines: arithmetic averages, dashed line: t_{90}

To determine the LCD of selected gases, they were diluted in 500 ppm or 100 ppm steps and compared to the air or nitrogen base line. The measurements were performed on freshly cleaned gold layers to guarantee the highest sensitivity, but this has the disadvantages of the large drift (see Section 4.5). Another difficulty relates to the inhomogeneity of the surface: different results for the LDC were achieved on different measuring spots. The lowest detectable concentration of methane, propane, carbon dioxide and hydrogen on gold layers are summarised in Table 4.1. These gases were chosen as representives for relevant gases which have to be detected in industrial applications. Carbon dioxide has to be monitored up to 7 % (v/v) in automobile industry, hydrocarbons and hydrogen up to their lower explosive limit (e.g. 4 % (v/v) for hydrogen) [1]. The required concentrations can be detected at this point with t_{90} values of a few seconds and therefore, the gas sensor is suitable for gas sensing application in principle.

Table 4.1: Lowest detected concentration (LDC) of selected gases on gold

Gas	LDC [ppm]
Methane	2000
Propane	2500
Carbon dioxide	8500
Hydrogen	700

However, gas concentrations in the low ppm range often have to be detected, e.g. 10 ppm of hydrocarbons in oil rigs. Therefore, an enhancement of the sensitivity is intended, which can be achieved by an additional sensor layer (see Section 5).

4.5 Ageing of gold layers

An important requirement of gas sensors is their physical and chemical stability over time. A change of the sensor surface, e.g. by chemical decomposition, would imply a change in the index of refraction, therefore a change in the position of the SPR effect and hence an instability of the initial value. An indication for the change of the gold surface is the location and the shape of the SPR effect. Indeed, the shape and the location of the Δ- and Ψ-AOI spectra change after some time when the gold layer is exposed to the laboratory atmosphere, see Figure 4.13. Right after the deposition of the gold layer, the Δ values extend from 300° to nearly 0° with a sharp jump at the SPR angle. Six weeks later the curve is smaller and the SPR effect shifted to higher AOI, which can be also observed in Ψ (not shown). This effect could be attributed to contaminations on the gold surface. It is possible to clean the surface chemically with the RCA method (see Section 3.2) to regain its initial state. The difference between the curve measured after deposition and the one measured after chemical cleaning is caused by the already discussed small surface inhomogeneities: after renewing the measuring arrangement (copper cell, glass slide, anisole, glass prism), the initial measuring spot is displaced and results in different measuring values.

Apart from the change of the SPR curve in the AOI dependent measurements, there is a drift towards higher Δ values in fixed AOI measurements on gold, as mentioned in section 4.3. The two phenomena are ascribed to contaminations like sulphides that bind covalently on the gold surface. The result of an experiment which confirms the supposition is presented in Figure 4.14. Here, 10 ppm hydrogen sulphide caused a significant gradient. The sulphuric atoms bind covalently on the gold surface, change its properties [47] and thus the Δ signal is irreversible.

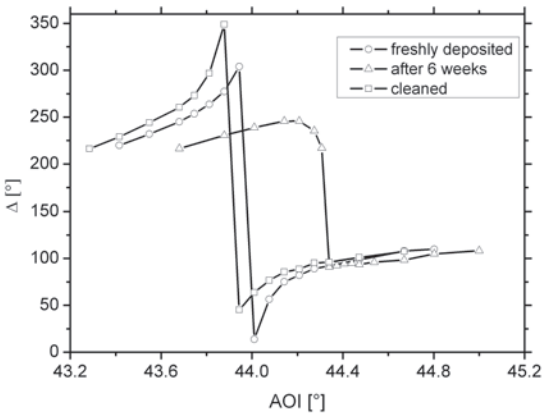

Figure 4.13: SPR effect of a 44 nm gold layer after deposition, after 6 weeks in laboratory atmosphere, and chemically cleaned with the RCA method

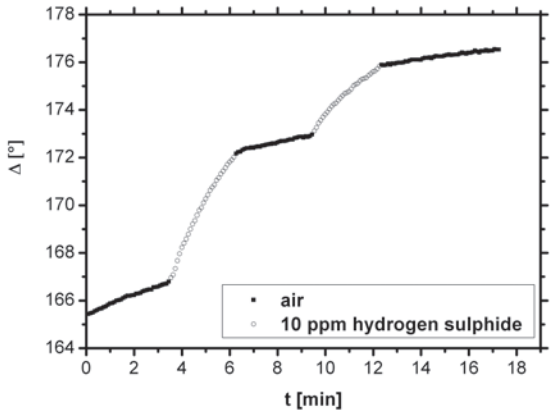

Figure 4.14: The irreversible increase in Δ when exposing the gold surface to hydrogen sulphide

The experiment shows on the one hand that the gold surface is susceptible to contamination and not applicable as a sensor surface in a laboratory atmosphere. On the other hand, it proves that the method is sensitive enough to monitor the growth of a monolayer of gold hydrosulfide. The contamination of the gold layer can be avoided by top-coating it with an additional protection layer as shown in the next section.

5 Top-coated gold layers

As shown in the prior section, gases can be distinguished based on their difference in refraction index by using gold layers as sensitive layers. Furthermore, the amplitude of the Δ response is dependent on the gas concentration. However, using bare gold surfaces poses the disadvantage of contamination and the resulting decrease of sensitivity. Therefore, it is reasonable to protect the gold layer with an additional layer. As found in literature, additional layers can also enhance the sensitivity. For example, self-assembled monolayers (SAMs) have been used. Thioalkanes are connected to the gold layer and if they are equipped with functional groups, the analytes can be adhered, the analyte concentration on the surface increases and the sensor response is improved [48, 49]. In this studies, organic materials such as SAMs and Langmuir-Blodgett (LB) layers have been tested, but it was observed, that the stability was insufficient, or the sensitivity degraded significantly compared with the uncoated gold layers. In addition, amorphous hydrocarbons (a-C:H) produced by chemical vapour deposition (CVD) were applied [50]. Obviously, this material degrades over time by releasing hydrogen and was therefore considered not applicable. The potential material for the top-coating of the gold layers has to be chemically stable against most gases and physically stable over a long time. Furthermore, it has to be a material which can be deposited on the nanometer scale, because any top-coating of the gold layers means lower sensitivity since the evanescent field of the surface plasmons is attenuated with growing distance to the gold surface. On the other side, it is imaginable that an additional layer would increase the sensitivity, e.g. when the specific surface area is enlarged to increase the number of adsorbed gas molecules or when the top-coating material catalyses chemical reactions. In this work, the focus for protection layers is on thin inorganic materials: TiO_2, ZrO_2, MgF_2, and $Fe : SnO_2$ have been tested.

5.1 Titanium dioxide TiO_2

One of the investigated materials concerning protection of the gold layers is TiO_2. It is a well investigated material also on nanometer scale due to its wide-ranging applications like in photovoltaics or photocatalytis [51]. There are many possibilities to synthesise TiO_2 nanostructures whereas in this work the sol-gel (SG) method as well as physical vapour deposition (PVD) have been used. This inorganic material was expected to be chemically inert against gases and to be stable over a long time [52]. Furthermore, it was expected to enhance the sensitivity due to the increased surface to volume ratio, which could allow the formation of an adsorptive layer. TiO_2 has been already applied as gas sensor based on the change of its electrical or optical properties [51].

5.1.1 Surface analysis

The TiO_2 top-coating layers were synthesised by PVD as well as by the SG method. Dependent on the synthesising process, thin layers with different optical and sensing properties were obtained. To gain a first impression of the surface qualities, the layers were investigated by SEM. The results of SEM measurements of a 10±2 nm TiO_2 layer produced by PVD deposited on a 43 nm gold layer (magnification: 30.000) and of a 5±2 nm TiO_2 produced by sol-gel process on a 42 nm gold layer (magnification: 50.000) are shown in Figure 5.1. The surface of the PVD TiO_2 shows a regular microstructure. There are regular elevations which have the same size. The SG TiO_2 layer does not show any microstructure even at a higher magnification. Obviously, the wet solution of the SG preparation fills the uneven structure of the gold layer and a flat surface is the result. The TiO_2 layers were also investigated with AFM (Data not shown). The average surface roughness R_a of different PVD TiO_2 layers was determined as between 1.6 and 4.2 nm and of different SG TiO_2 layers between 0.9 and 1.1 nm. This affirms the flatter structure of SG TiO_2.

Figure 5.2 shows the layer structure of a BK7/Au/TiO_2 (PVD) system analysed by transmission electron microscopy (TEM). The thin TiO_2 layer is clearly

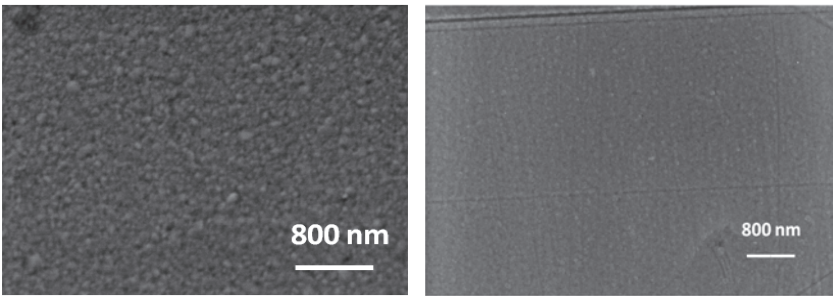

(a) 10±2 nm TiO_2 (PVD) on 43 nm gold, magnification: 30.000

(b) 5±2 nm TiO_2 (SG) on 42 nm gold, magnification: 50.000

Figure 5.1: SEM images of TiO_2 produced by PVD and SG respectively

visible as a homogenous layer covering the gold surface. The chromium layer above has been deposited to stabilize the system and for preparation. The thickness of the gold layer is 50 nm and the thickness of the TiO_2 layer is 11 nm. Between gold layer and glass slide, a small interface can be distinguished which is assumed to be the NiCr adhesive layer.

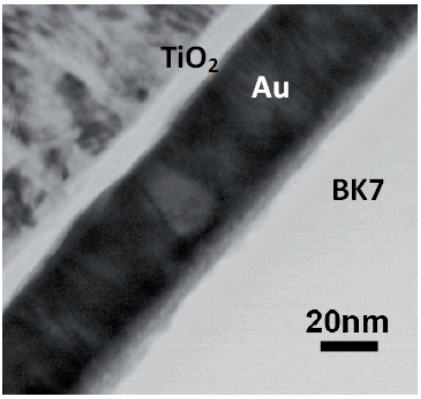

Figure 5.2: TEM cross-section of a gold layer on BK7 coated with PVD TiO_2

To investigate the TiO_2 material produced by PVD and SG concerning its optical properties, layers with different thicknesses (5, 10, 20 and 50 nm) have

been deposited on silicon and investigated by SE mapping in order to compare them. The results for all layers should serve to develop an adequate general model for the system BK7/Au/TiO_2. The experimental data of the dispersion of the ellipsometric angles Ψ and Δ of 10 nm TiO_2 (PVD) and 10 nm TiO_2 (SG) on Si are compared in Figure 5.3. Due to the differences of the experimental results, different optical models are required. Modelling the 10 nm TiO_2 (PVD) led to a MSE value of 3.4 by using the following model (top to bottom):

TiO_2 (three Gauss oscillators)
silicon as bulk phase [53]

Modelling and fitting the TiO_2 (SG) layers (any thickness) resulted in good MSE values of not more than 2. The following model was constructed:

TiO_2 (one Tauc-Lorentz oscillator)
silicon as bulk phase [53]

The generated data for both layers is marked in Figure 5.3 as circles. The resulting dispersions of the optical constants are presented for the PVD and the SG TiO_2 layer respectively in Figure 5.4. The progression of the index of refraction is similar, but differs in the visible and IR region: PVD TiO_2 has higher values compared to SG TiO_2. Both TiO_2 types have a maximum in the index of refraction at about $\lambda = 300$ nm, whereas n_{300}(PVD TiO_2) = 2.8 and n_{300}(SG TiO_2) = 2.4. The index of refraction at the wavelength applied for gas sensing measurements is $n_{632.8} = 1.95$ for the SG layer and $n_{632.8} = 2.1$ for the PVD layer. This value is according to literature values, where indices of refraction $n_{632} = 1.74$-1.9 for TiO_2 synthesised by airosol gel process at low temperatures have been reported [54]. The indices of refraction at $\lambda = 500$ nm are lower ($n_{500} = 2.2$ (PVD) and $n_{500} = 1.98$ (SG)) as reported for TiO_2 in literature: $n_{550} = 2.56$-2.72 for layers produced by filtered arc deposition [52], $n_{500} = 2.8$ for layers produced by RF magentron sputtering [55]. This is not untypical, since the refractive index strongly depends on the process parameters.

The extinction coefficient however shows a different dispersion dependent on the production process: the SG TiO_2 layer is transparent above $\lambda = 345$ nm,

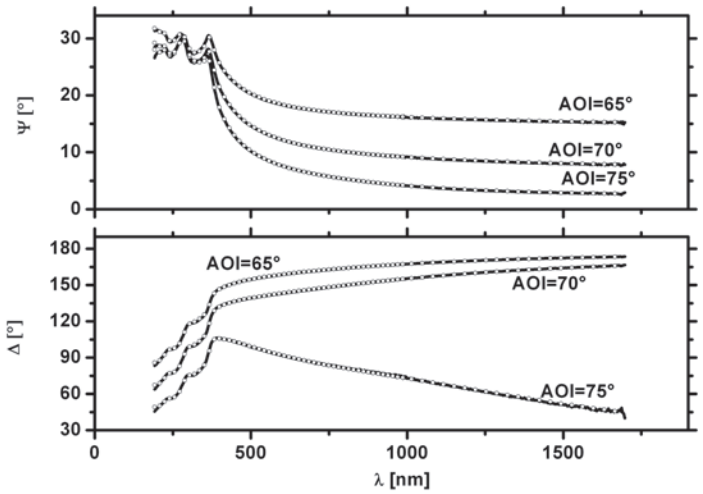

(a) 10.8 nm TiO_2 (PVD) on Si

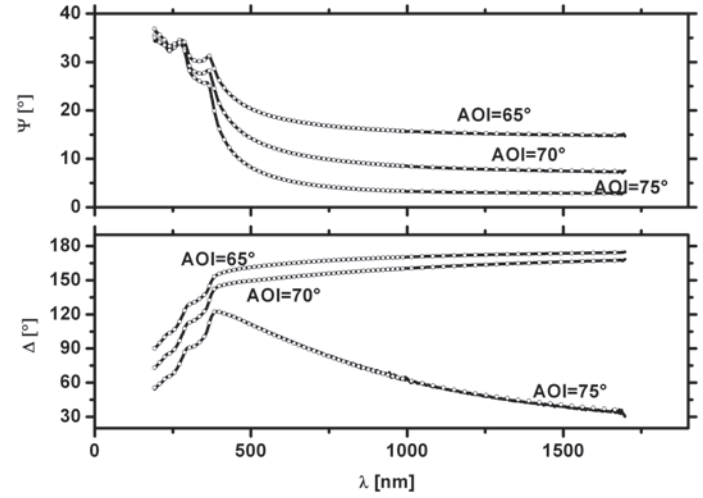

(b) 7.8 nm TiO_2 (SG) on Si

Figure 5.3: Solid lines: measured, and circles: generated ellipsometric angles of TiO_2 produced by PVD and SG respectively

whereas the absorption of the PVD TiO_2 layer increases again above $\lambda = 450$ nm. Since the PVD process happens at room temperature under oxygen deficiency conditions, non-stoichiometric TiO_{2-x} layers are the result. The absorption in the visible region is due to the existing Ti^{3+} ions resulting from the vaporisation of Ti_3O_5 and which absorb in the region of visible light [56]. The untypical absorption in the IR region could be explained by finely dispersed metallic titanium. The thickness of the layers was determined for every measuring spot in the SE mapping. The values vary for 1 - 2 nm and in the following discussion, the thickness value determined for the centre measuring spot is quoted.

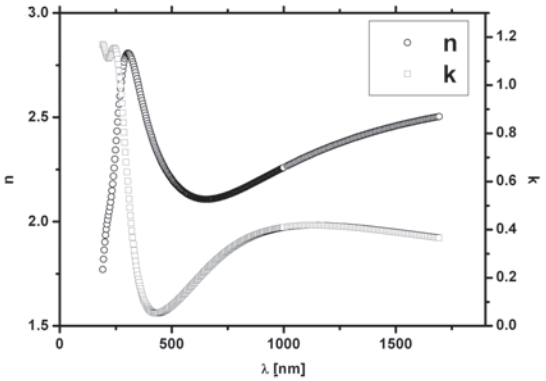

(a) 11 nm TiO_2 (PVD) on Si

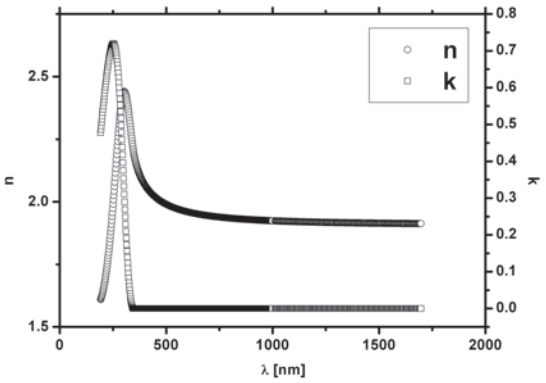

(b) 8 nm TiO_2 (SG) on Si

Figure 5.4: Optical constants of TiO_2 produced by PVD and SG respectively.

5.1.2 Theoretical consideration of the SPR effect

The location and the shape of the SPR effect (Ψ- and Δ-AOI spectra) of a BK7/Au system has already been discussed in Section 4. The SPR effect on a gold layer is expected to be influenced by top-coating with an additional

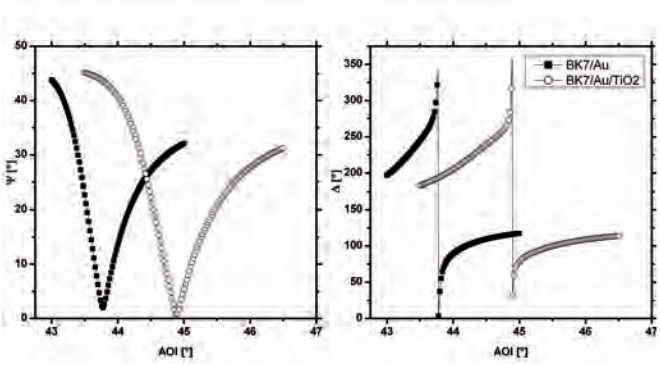

Figure 5.5: Comparison of the simulated SPR effect on gold and gold coated with 5 nm TiO_2, guidelines added

layer. To estimate this change, a simulation of the SPR effect was made (see Section 3.3). The layer system model for an uncoated gold layer consisted of the following components (top to bottom):

BK7 as ambient [41]
4.7 nm NiCr (determined by SE mapping of NiCr layers on Si)
43 nm gold (three Gauss and one Drude oscillators)
vacuum (ϵ_1=1 for vacuum, $\epsilon_2 = 0$)

The model for the top-coated gold layer consisted of:

BK7 as ambient [41]
4.7 nm NiCr (determined by SE mapping of NiCr layers on Si)
43 nm gold (three Gauss and one Drude oscillators)
5 nm TiO_2 (three Gauss oscillators, based on the SE results for Si/TiO_2)
vacuum (ϵ_1=1 for vacuum, $\epsilon_2 = 0$)

The results of the simulation are presented in Figure 5.5. When introducing the TiO_2 between gold and vacuum, the location of the SPR effect is shifted for 1.1° to higher AOIs, which has to be considered in the practical performance of the experiments. The shape of the Ψ as well as the Δ curve on the other hand remains the same, thus no loss of sensitivity was expected.

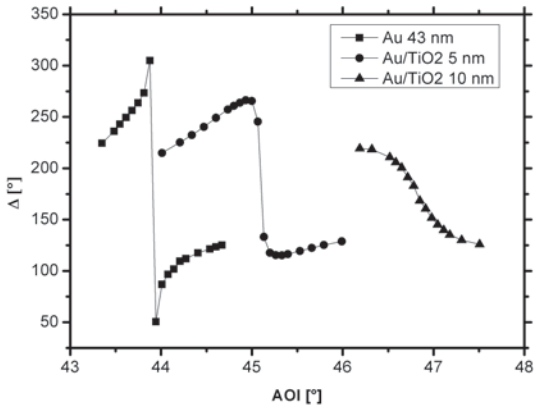

Figure 5.6: Comparison of the SPR effect on Au, Au coated with 5 nm and Au coated with 10 nm TiO_2 respectively, guidelines added

5.1.3 Experimentally determined SPR effect

As shown by the simulation in the prior section, the top-coating of the gold layer with an additional layer causes a change in the SPR curve concerning the AOIs. The experiment confirms this theoretical estimate, as can be seen in Figure 5.6. The Au-SPR curve was measured on a freshly cleaned 43 nm gold layer. The SPR curve on the same Au layer top-coated with 5 nm TiO_2 (PVD) is softer and shifted to higher AOIs (central curve). In contrast to the simulation, not only the location, but also the shape of the Δ-AOI-curve changed. This is due to the damped excitation of SPs, which could not be considered in the simulation, where the ideal case is considered. In reality, the inhomogeneity of the layer and other irregularities differing from an ideal case are given. The right curve in Figure 5.6 was measured on a 10 nm TiO_2 (PVD) layer that was deposited on a 43 nm gold layer. The SPR effect is clearly reduced: the gradient is smaller, the curve softened and measurements confirmed the low sensitivity.

The expected advantage of the additional layers is the improvement of stability, since the contamination of the gold layer can be avoided. The stability of a

BK7/Au/TiO_2 system was investigated for a period of 4 months. In this time the sensor system was exposed to different analyte gases (methane, propane, carbon dioxide, carbon monoxide) and as can be seen in Figure 5.7, the SPR effect is not influenced at all.

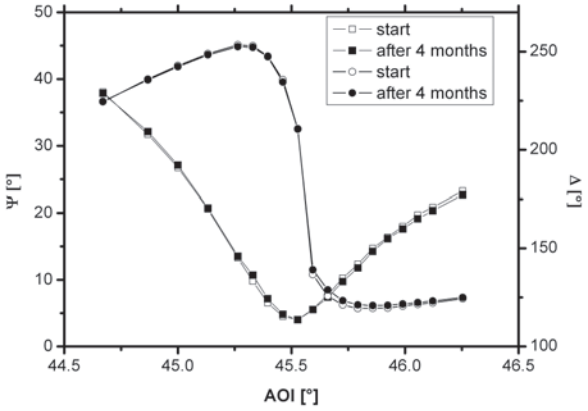

Figure 5.7: SPR effect of a TiO_2 layer (PVD, 7 nm) on Au short after deposition and after 4 months, guidelines added

To prove the protection effect of the TiO_2 layer, the sensor system was exposed to hydrogen sulphide. As shown in Section 4.5, 10 ppm hydrogen sulphide caused an irreversible increase of the Δ values on an unprotected gold layer. In contrast, the exposure of the sensor system Au/TiO_2 to even 50 ppm hydrogen sulphide cause an increase, but the values decrease to the base line after purging with air. Hydrogen sulphide does not destroy or contaminate the TiO_2 layer. Therefore, PVD TiO_2 is suitable for use as a protection layer. Comparable results were achieved for the SG TiO_2 protection layers. There is an efficient chemical and physical protection of the Au layer by top-coating with TiO_2.

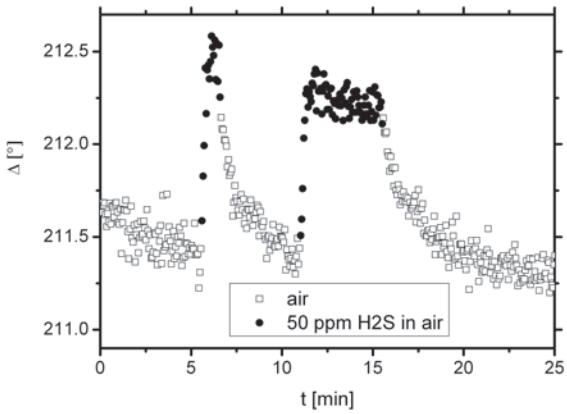

Figure 5.8: Exposure of a TiO_2 layer (PVD, 7 nm) on Au to 50 ppm hydrogen sulphide

5.1.4 Gas sensing

Not only the long-term stability, but also the sensitivity to gases can be enhanced by top-coating the gold layer with TiO_2. To compare the sensitivity between unprotected and protected gold, the same measurements were performed first on a freshly cleaned gold layer and second on the same sample after deposition of TiO_2. Figure 5.9 presents the results of a hydrogen detecting fixed AOI measurement on a 49 nm Au layer and on the same Au layer top-coated with a 3.5 nm SG TiO_2 layer.

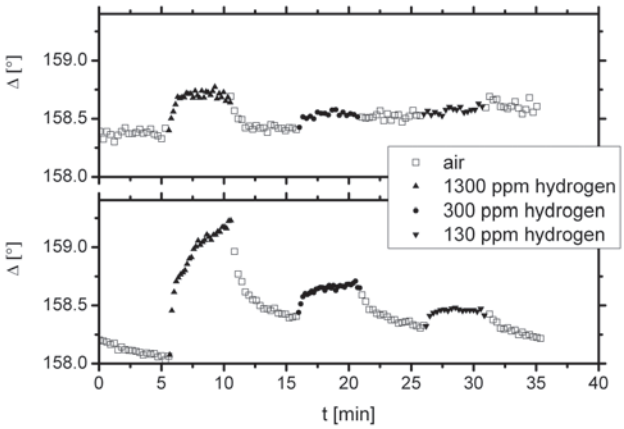

Figure 5.9: Different concentrations of hydrogen in air on Au, AOI = 43.81° (top) and on a Au/TiO_2 system, AOI = 44.74° (bottom), volume flow rate 100 ml/min. Data removed for clarity

Both measurements were carried out in the same Δ range with the same volume flow rate. The first obvious difference is the different drift behaviour of the Δ values. The base line of the reference gas air increases by 0.2°/min during the measurement on Au. The base line on TiO_2 decreases by 0.03°/min and it is shifted after the first hydrogen pulse from 158° to 158.5°, but stable or approximating the initial values respectively during the rest of the measurement. The second difference is the response of Δ to the different gas concentrations. On TiO_2 the increase is six times higher (158.0° to 159.2°) than on pure gold (158.4° to 158.6°) in case of 1300 ppm hydrogen. The other pulses with 300 and 130 ppm respectively are lost in the noise of the base line on gold, whereas on TiO_2 both peaks can be seen clearly. The third difference is the shape of the peaks. The values for 1300 ppm hydrogen on gold end in a linear plateau, on TiO_2 the final value is not reached within the 5 minute pulse, but approximated slowly. The simultaneous mechanisms responsible for gas sensing here are supposed to be the same as those on gold layers (see Figure 4.7) plus

catalytical reactions:

1. the **change in the index of refraction** in the analyte volume. There is no interaction between analyte gas and the sensor surface
2. the **formation of an adsorbed layer**. The gas atmosphere is thus denser next to the surface and the index of refraction increases
3. the **diffusion of the analyte gas** into the sensor layer
4. the **solvation of the analyte gas** in the sensor layer
5. **chemical processes** like catalytical reactions, as TiO_2 is known for its photocatalytic activity ([57])

The limiting factor is in this case the adsorption and the diffusion into the nanopores of the TiO_2 layer. The consequence is the modifying of the optical constants and the stronger response in Δ. This supposition is supported by the fact, that the base line does not reach the initial values after the first hydrogen pulse (Figure 5.9): By the end of the first pulse of hydrogen, the molecules are adsorbed on the layer surface and diffused into the layer. When switching again to the reference gas, the hydrogen molecules are displaced by oxygen and nitrogen molecules, and the trend of the base line towards the initial value can be clearly observed. Obviously, some hydrogen molecules remain inside the layer, occupy the adsorption sides inside the nanopores or are dissolved and prevent the decrease of the base line to the initial value. Although the SEM measurements showed flat layers without microstructure, SG TiO_2 is known to be porous, whereas the porosity decreases with increasing calcination temperature, since the material contracts and condenses due to water elimination [58]. The calcination temperature of the SG TiO_2 presented here is only 100 ℃, thus a porous structure can be expected, although the layer is extremely thin. Furthermore, nanomaterials are known to enlarge the surface to volume ratio when the material size decreases [51]. The gas measurements on PVD TiO_2 layers showed similar results concerning the sensitivity to gases (not shown). On these layers, the formation of an adsorption layer is very

likely due to the structured surface, which provides a high surface to volume ratio. Gas diffusion into the layer is also probable. To summarise, all detection mechanisms described above will occur simultaneously to a greater or lesser degree depending on the analyte gas and the surface qualities of the sensitive layer. The modification of the gold layer by top-coating with an additional layer TiO_2 contributes to the sensitivity of the sensor.

With fixed AOI measurements as shown in Figure 5.9, the response of Δ to low concentrations of gases has been investigated (compare lowest detected concentrations on gold, section 4.4). Due to inhomogenities on the surface, every measuring spot yields different results concerning the sensitivity of the Δ values. As example for this difference between the spots, two measurements at two different spots on the same layer (SG TiO_2) are shown in Figure 5.10. On one spot (Figure 5.10, left), a low concentration of hydrogen (5 ppm in nitrogen) gas cause about 0.75° increase in Δ. On another spot (Figure 5.10, right), 250 ppm of hydrogen cause only about 2° change in Δ, although the concentration is 50 times higher.

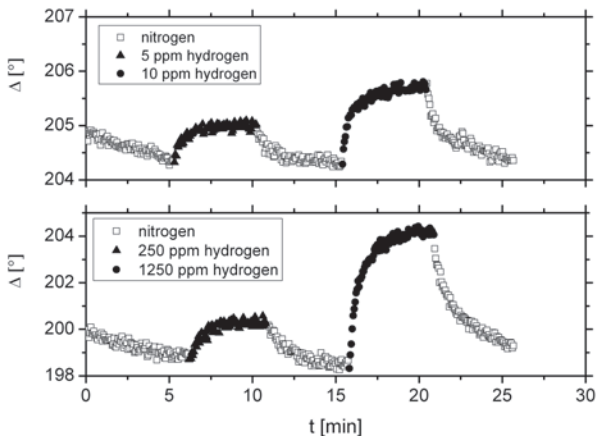

Figure 5.10: Different concentrations of hydrogen on the same SG TiO_2 layer detected on two different measuring spots. Data removed for clarity

On SG TiO_2 as well as on PVD TiO_2 layers the response of the sensor system to low concentrations have been examined on three measuring spots each. Selected gases have been diluted with the reference gas (nitrogen or air) in concentration steps of 10 or 5 ppm determining that the lowest concentration causing a change in the Δ values differs three σ from the base line (see Table 5.1). The LDC of hydrogen has been determined to 5 ppm, although the measurement in Figure 5.10 indicates that a detection of lower concentrations is feasible. The mixture of low concentrations is limited by the analyte gas and the mixing device (MFC) utilised.

Table 5.1: Lowest detected concentrations (LDC) of selected gases on PVD and SG TiO_2

Gas	LDC/ppm	
	PVD TiO_2	SG TiO_2
Methane	90	15
Propane	120	50
Carbon dioxide	170	85
Hydrogen	25	5

Obviously, the production process of the layers influences the material structure and therefore the sensitivity to gases. The indices of refraction determined by ellipsometry of the SG TiO_2 is lower ($n_{632.8} = 1.95$) than of the PVD TiO_2 ($n_{632.8} = 2.1$), i.e. it is less compact and can allow more pore diffusion or the surface to volume ratio is higher. Furthermore, the PVD TiO_2 layers are produced under oxygen deficiency conditions and show therefore a small extinction in the Vis-IR region in contrast to the SG TiO_2. This difference in the chemical structure of the PVD and SG TiO_2 layers could also be the reason for the difference in the determined LDCs. It is certain that the production process and the choice of the measuring spot influence the sensitivity to gases. This is important for a potential application.

5.2 Zirconium dioxide ZrO_2

Zirconium dioxide (ZrO_2) is a widely used material due to its chemical inertness, thermal stability and high permittivity [59, 60]. It is applied in ceramics technology, as a semiconductor, in photocatalysis, and in heterogenous catalysis for reactions like paraffin isomerization, hydrogenation of olefins, and alcohol dehydrogenation [61]. Furthermore, ZrO_2 is used in sensors, e.g. for monitoring humidity [62], hydrogen peroxide [63] or biomolecules [64]. It has also proven its applicability as gas sensor e.g. to measure oxygen for the control of combustion processes in vehicle engines [65] and it has an affinity to carbon dioxide [59]. Therefore, it is an adequate material to protect the gold layers and to enhance the sensor sensitivity at the same time. ZrO_2 can be produced by different methods, e.g. atomic layer deposition (ALD) [60] or PVD [66]. In this work, the SG method has been used. ZrO_2 produced by the SG method is a material with a high surface area, which is expected to allow the formation of an adsorption layer [67].

5.2.1 Surface analysis

Figure 5.11 shows a SEM image of a ZrO_2 surface deposited by the SG process on a gold layer measured by SEM in a magnification of 100,000. The image shows a nanostructure with agglomeration of material in small plates with a diameter under 100 nm. The wet precursor is dispersed over the sample by spin coating and when drying, ZrO_2 isles are formed. The isle structure is confirmed from AFM measurements as shown in Figure 5.12, where small agglomerations can be seen clearly (average roughness $R_a = 1.2$ nm). Also in literature, SG ZrO_2 samples which show agglomerates of very small and round particles are described [61]. The presented SEM and AFM measurements are from different samples for preparation reasons, but as the ZrO_2 layers have been prepared under the same conditions, a similar structure is assumed for all layers produced.

The inhomogeneous ZrO_2 surface gives rise to some disadvantages. First, the layer was intended to protect the underlying gold layer from contamination

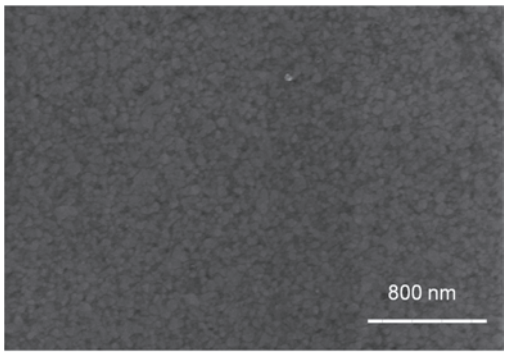

Figure 5.11: SEM image of a ZrO_2 layer deposited on gold

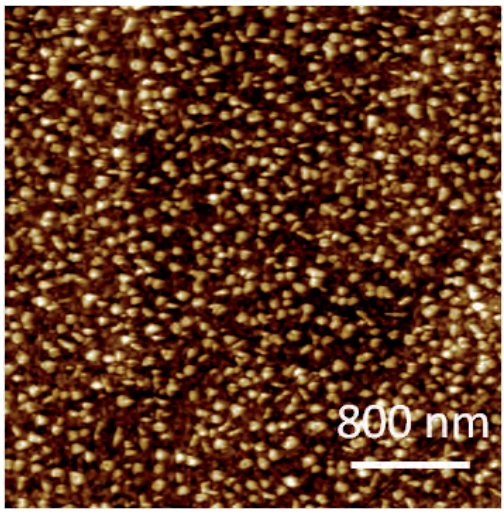

Figure 5.12: AFM image of a ZrO_2 layer deposited on gold

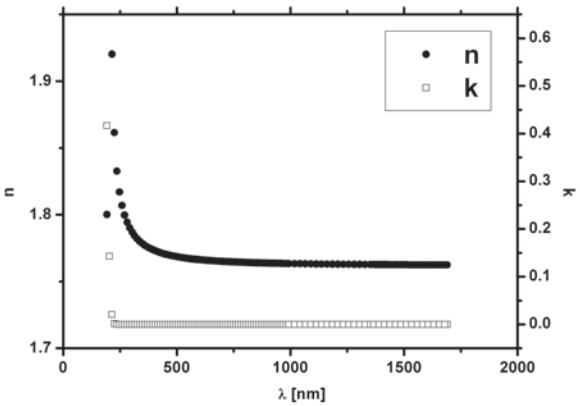

Figure 5.13: Optical constants of a ZrO_2 layer deposited on gold.

with pollutants in the atmosphere, therefore it has to cover the gold surface. Due to the forming of separate isles, the coverage with a closed layer is not given and thus the protection of the gold layer is not expected. Second, the investigation by SE is difficult, as the laser spot (diameter 5 mm) of the M2000 ellipsometer, which has been used for surface analysis, includes the inhomogeneities. However, the ZrO_2 layers deposited on gold were characterised by SE mapping. The following general model was used for the analysis (top to bottom):

ZrO_2 (one Tauc-Lorentz oscillator)
43 nm gold (one Drude and three Gauss oscillators)
2.6 nm NiCr (determined by SE mapping of NiCr layers on Si)
BK7 [41]

The layer was mapped on 9 different measurement spots and the generated data was fitted to the experimental data at every point. The resulting MSE ranged between 8.4 and 16.6, but high MSE values were expected due to the irregular surface. The optical constants are presented in Figure 5.13.

Compared to values in literature, the index of refraction is lower: $n_{580} = 1.77$

and n_{600} = 1.77 for the SG layers presented here, but n_{580} = 1.8 - 2.2 for ZrO_2 produced by ALD, whereas the index of refraction depends on growth parameters like the deposition temperature [68], and n_{600} = 1.95 for ZrO_2 produced by PVD [66]. Absorption occurs only in the UV region, but decreases rapidly and disappears above 220 nm. This is in accordance to literature [61, 66]. The determined thicknesses of the layers vary strongly depending on the measuring spot. The quoted values in the following are the ones for the centre of the layer.

5.2.2 Experimentally determined SPR effect

As shown in Section 5.1, coating of the gold layer with an additional layer causes a shift of the location of the SPR effect to higher AOI. The expected shift also occured in case of ZrO_2. Figure 5.14 shows the SPR effect on a gold layer and on the same gold layer coated with ZrO_2. The coating causes a shift of 1° to higher AOIs. For clarification of the inhomogeneity and the resulting problems, the SPR effect is plotted for two different measuring spots. The two curves lie in the same AOI range, i.e. the thickness of the layer is nearly the same. But the minimum difference in Ψ is 7° and the Δ curve differs. Although the AFM picture (Figure 5.12) shows no closure in the ZrO_2 layer, the measurement of the SPR effect shows the presence of an additional layer, i.e. the SPR minimum lies above 45° at every measuring spot. This is due to the large size of the laser spot of the employed SE400 ellipsometer (diameter about 2 mm) compared to the particle size: it ensures many of the ZrO_2 isles and the measured ellipsometric angles are the result of the average on every specific measuring spot. Due to the different size and the inhomogenous dispersion of the isles, the measured values differ strongly dependent on the measuring spot. The ZrO_2 layer has been deposited on gold in order to prevent contamination and thus to stabilise position and shape of the SPR effect. The SPR effect on a ZrO_2 layer shortly after deposition and after one year is shown in Figure 5.15. The position has not changed at all, only the minimum in Ψ changed for 1.3°.

Due to the inhomegenities on ZrO_2 layers discussed above, it is difficult to

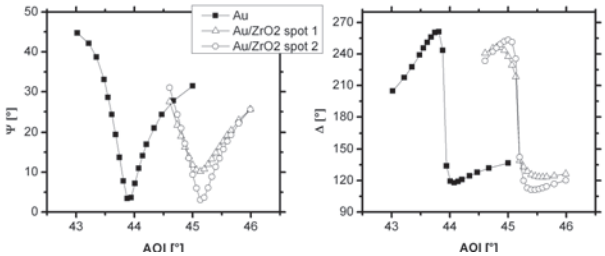

Figure 5.14: SPR effect on Au and on Au/ZrO_2, λ=632.8 nm

make a statement about the stability of the overall layer, since every spot on the layer gives different results. The difference of the two curves in Figure 5.15 could also be caused by surface irregularity. The SPR effect has been quantified right after deposition on several measurement spots and has been checked regularly over the year with similar results. The change over time was always smaller than the shift due to inhomogeneity. Therefore, it can be assumed that in general the surface does not change much and the gold layer is protected at least partly. To investigate the fractional change on the surface in detail, the laser spot should be of the size of the agglomerated isles (< 100 nm).

5.2.3 Gas sensing

Gas sensing on ZrO_2 is similar to TiO_2 (see Section 5.1) concerning the progression of the Δ values and sensitivity. The change in Δ is not abrupt, but axproximating a plateau. Therefore, similar mechanisms are assumed to occur: 1. change in the index of refraction of the gas phase, 2. formation of an adsorption layer, 3. diffusion of the gas into the layer, 4. solvatation of the gas inside the layer, and 5. catalytical reactions at the same time. Mechanism 1 is obvious, mechanism 2 is supported by the fact that the formation of an adsorption layer is promoted by the high surface area of SG ZrO_2 layers, which provides many adsorption sites. The surface area decreases with increasing calcination temperature due to densification of the material [61, 67]. As the calcination temperature of the layers presented here is low (100 ℃), a

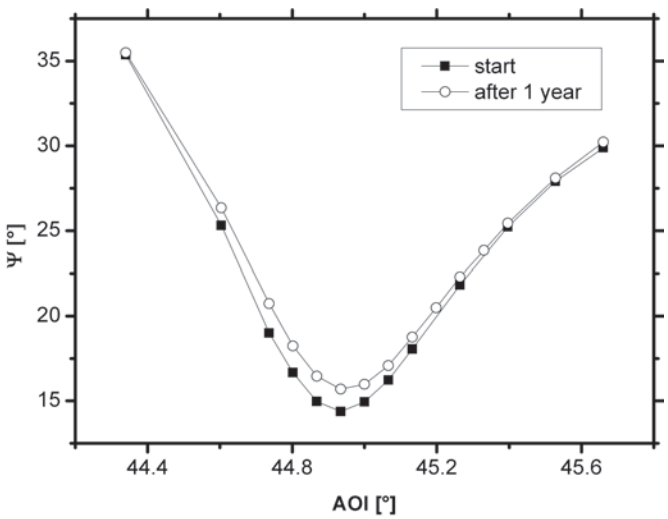

Figure 5.15: Change in SPR effect on a ZrO_2 layer deposited on gold

high surface area is given. Furthermore, the adsorption of gases on the ZrO_2 surface is e.g. used in oxygen sensors [69] and the affinity to the gas carbon dioxide, bound by bidentate coordination to the zirconium ions, is known [59]. Mechanism 3, i.e. the penetration of the layer with the gas, is indicated by the results of a measurement with different concentrations of hydrogen, presented in Figure 5.16. It shows the time dependent detection of pure and diluted hydrogen and methane respectively on 9 nm ZrO_2. In case of hydrogen, the response of the Δ values is interesting: 3 % hydrogen cause a peak towards higher values, 100 % towards lower values. Obviously, different mechanisms on the sensor surface dependent on the hydrogen concentration are the determining factor. The decrease in the second hydrogen peak is assumed to be the change in the refractive index of the gas phase. The lower index of hydrogen compared to the reference gas nitrogen effects the shift of the location of the SPR effect to lower angles of incidences and thus the Δ values decrease in the fixed AOI measurement. Increase of Δ, as in case of 3 % hydrogen, would mean a shift of the SPR minimum to higher AOI and a higher index of refraction respectively. This means the physical properties of the ZrO_2 layer have changed

which happens when hydrogen molecules diffuse into the layer or adsorb on the surface. This effect is also the reason for the delayed response in the 100 % peak: hydrogen molecules change the surface which means increase of Δ, but the decrease of the index of refraction in the gas atmosphere due to the high hydrogen concentration is the stronger effect, which is only slowed down by the penetration. The same mechanisms take place in the case of methane, but here the signal is enforced because both, change of index of refraction in the gas atmosphere and change of index of refraction of the sensor layer cause a shift of the SPR effect in the same direction.

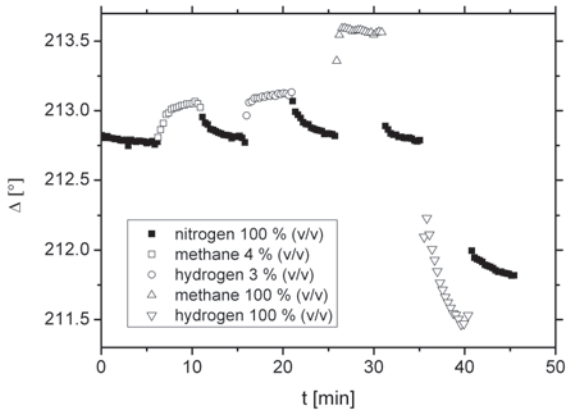

Figure 5.16: Detection of different concentrations of hydrogen and methane on 9 nm ZrO_2

Not only the formation of an adsorption layer and the penetration of the gases are assumed to build the basis of gas sensing, but catalytic processes are also thought to play a role on the ZrO_2 surface. ZrO_2 is used as a catalyst: among other reactions, the synthesis of hydrocarbons from carbon monoxide and hydrogen is catalyzed, whereas the selectivity is affected by the preparation method [69]. Therefore, catalytic oxidation or reduction respectively of the analyte gases can happen on the sensor surface and the products can contribute to the change of the index of refraction.

The adsorption of gases on the ZrO_2 surface as well as the diffusion of the gases into the layer and probable catalytic reactions enhance the sensor sensitivity compared to the unprotected gold surface. The LDCs of several gases have been determined and are summarised in Table 5.2. Of course the irregular surface leads to different results dependent on the measuring spot, but the experiments have been repeated several times and LDCs have been determined in the low ppm range.

Table 5.2: Lowest detected concentrations (LDC) of selected gases on ZrO_2

Gas	LDC [ppm]
Methane	15
Propane	50
Carbon dioxide	85
Hydrogen	15

The applicability of thin SG ZrO_2 layers as sensor layers has been successfully proven. Although the SG process provides no closed layers, but surfaces with isles-like structure, the SPR effect is stable on gold layers deposited with ZrO_2 and the sensor sensitivity is enforced compared to uncoated gold layers.

5.3 Magnesium fluoride MgF_2

Magnesium fluoride (MgF_2) is a hard and durable material, which is already used in long range surface plasmon resonance (LRSPR) or fibre optic SPR sensors [70, 71]. It is known as a dielectric in multilayer systems and as a catalyst for organic reactions [34, 72]. MgF_2 can be produced in thin layers by e.g. electron beam evaporation [73] or sol-gel (SG) process, where a high surface area is achieved [74]. In this work, SG MgF_2 has been used as protective layer on gold and in order to enhance the sensitivity to gases.

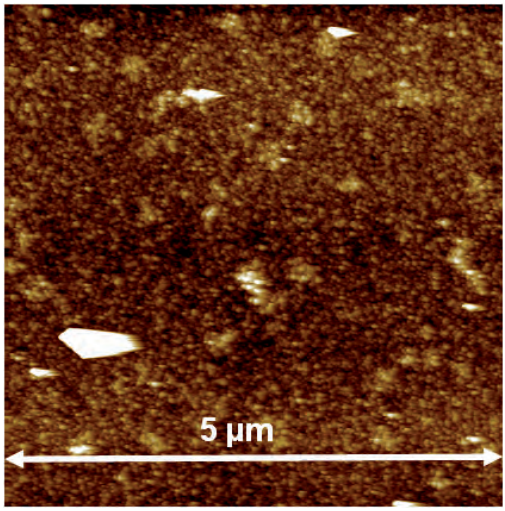

Figure 5.17: AFM image of a MgF_2 surface deposited on gold

5.3.1 Surface analysis

The thin SG MgF_2 layers were investigated by SEM and AFM. SEM measurements show flat layers without any microstructure (data not shown), and the results of AFM measurements (see Figure 5.17) confirm a nanostructure with a closed layer consisting of round particles distributed homogeneously with nearly the same size and sporadic agglomerations. The large white areas are dust or other contamination particles. Although the average roughness is very low ($R_a = 1.5$nm), every measuring spot will provide slightly different results, comparable to the other materials discussed above. In general, the SG produced MgF_2 layers are expected to provide a large surface area and to allow the building of an adsorption layer which contributes to the enhancement of the sensor sensitivity.

SG MgF_2 layers were deposited on Si in order to investigate them by SE mapping. The dispersion of the ellipsometric angles has been quantified for different measuring spots and the following general model has been used for analysis (top to bottom):

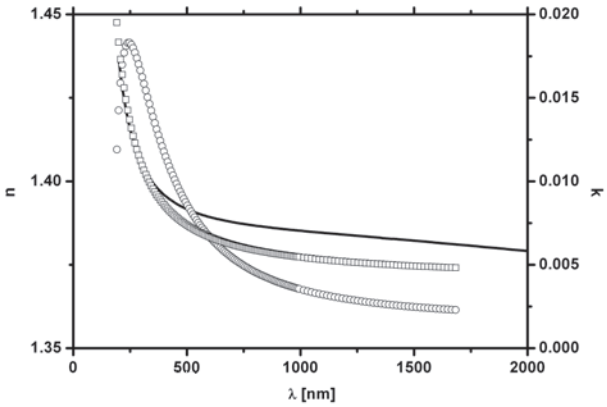

Figure 5.18: Optical constants of a 7 nm thick MgF_2 surface deposited on Si. Solid line: literature values for n [42]

MgF_2 (Cauchy material)
silicon [53]

Fitting the model to the experimental data of different measuring spots resulted in good MSE values between 3.4 and 2.0. The optical constants are shown in Figure 5.18, compared with literature values [42].

Besides the plotted values, there are other well-fitting values in the literature, e.g. the values $n_{500} = 1.38$ [33, 75] or $n_{830} = 1.38$-1.39, dependent on the relative humidity of the atmosphere, are reported [18]. The here determined values are $n_{830} = 1.37$ and $n_{500} = 1.39$. As expected from literature values [42], the absorption is very low, but increasing for a layer thickness of 20 nm (data not shown). On the basis of these results, the optical constants and thicknesses of the MgF_2 layers deposited on gold and applied for gas sensing could be determined.

5.3.2 Experimentally determined SPR effect

As shown in sections 5.1 and 5.2, deposition of an additional layer on the gold layer will cause a shift of the location of the SPR effect to higher AOIs. Coating the gold layer with MgF_2 causes a shift of about 0.5° as well, see Figure 5.19, where the Ψ-AOI-spectra of an uncoated gold layer and the same gold layer protected with 6 nm MgF_2 is presented. As mentioned above, every measuring spot differs slightly from the other due to the inhomogeneity of the surface, but in general the shift of the location is in the same scale. The change over time of the location or the shape of the SPR effect respectively, is an indicator for change of the top-layer due to degradation or contamination. Long term measurements prove the stability of the layer over months and thus the applicability as a protective layer for gold (see Figure 5.19). The slight difference of the two SPR curves on MgF_2 is within the range expected from the surface inhomogeneity.

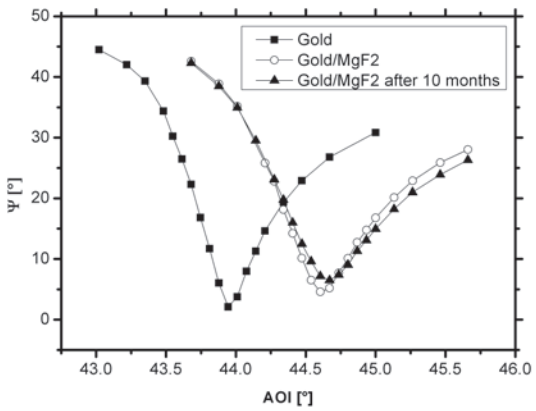

Figure 5.19: Shift of the SPR effect on gold by top-coating with 6 nm MgF_2 and the ageing of the layer

5.3.3 Gas sensing

Not only the stability of the sensor system, but also the sensitivity was expected to be enhanced by SG MgF_2 layers. As can be seen in Figure 5.20, which shows a comparison of time dependent measurements with the analyte gas carbon dioxide and the reference gas air on gold and MgF_2 top-coated gold, the additional layer provides some advantages: The noticeable drift on gold, due to permanent adsorption of contaminations on the surface is suppressed by the top-coating. Furthermore, the peaks in Δ caused by the analyte gas are clearer and higher on MgF_2. As with the other coating materials, an adsorption process is assumed due to the asymptotic response in Δ. Furthermore, as on the other materials a combination of different sensing mechanisms takes place: change in the refractive index in the gas phase, formation of an adsorption layer on the MgF_2 surface, diffusion of the gas molecules into the layer, and solvatation of the gas inside the layer. Due to the diffusion phenomenon MgF_2 has been proposed as a transducing medium in optical fibre sensors: it binds water vapor and the refractive index changes [18].

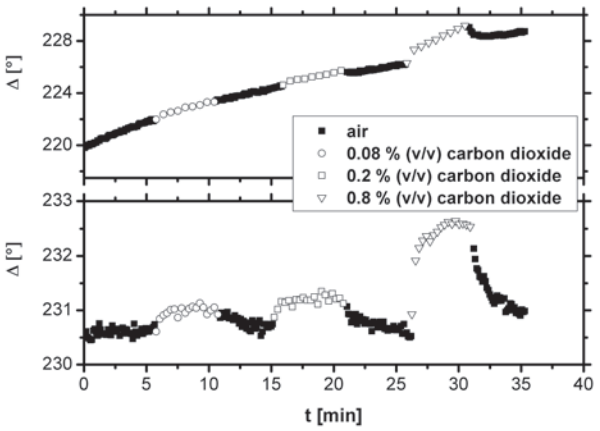

Figure 5.20: Comparison of the detection of different carbon dioxide concentrations on Au (top) and on Au/MgF_2 (bottom)

The results for sensing gas of low concentrations on MgF_2 protected gold layers are similar to the materials discussed above (TiO_2 and ZrO_2). The sensitivity to low concentrations has been determined by diluting the accordant analyte gases and quantifying the Δ response on different measuring spots in order to include the differences resulting from the surface inhomogeneity. The lowest detected concentrations (LDC) for selected gases are summarised in Table 5.3.

Table 5.3: Lowest detected concentrations (LDC) of selected gases on MgF_2

Gas	LDC [ppm]
Methane	100
Propane	50
Carbon dioxide	150
Hydrogen	5

Thin SG MgF_2 layers do not only stabilize the sensor system, but also enhance the detection of low gas concentrations. They are therefore suitable as a sensor material.

5.4 Iron doped tin oxide Fe:SnO_2

An investigated material concerning enhancement of sensitivity is iron doped tin oxide $Fe : SnO_2$. Tin oxide (SnO_2) is already well known as a component in semiconductor gas sensors. The gas sensing effect is based on catalytic oxidation of the analyte gas on the metal oxide film. Gas particles, also oxygen ions from the surrounding area, adsorb at the surface and a following reaction leads to a change in the electric resistance, which is related to the gas concentration [76, 77]. Semiconductor gas sensors normally work at a temperature of 200 ℃. But if the metal oxide is doped with iron, sensing of e.g. hydrogen sulphide becomes possible at room temperature [78]. Furthermore, $Fe : SnO_2$ based semiconductor sensors have been found to be sensitive to the toxic gas carbon monoxide, where the iron content has an influence on the sensitivity [13]. Also SnO_2 has been used to perform SPR measurements concerning gas

sensing [15]. These facts led to choose $Fe : SnO_2$ as a coating material which could also improve sensitivity particularly for carbon monoxide sensing.

5.4.1 Surface analysis

SEM measurements of $Fe : SnO_2$ (see Figure 5.21) show flat surfaces with very low roughness and some isolated visible larger particles, which can be pillars or spherical caps [36]. The total iron atomic concentration was calculated by XPS to ∼2 at.% with a precision of ∼0.5 at.% for all samples (data not shown) [79].

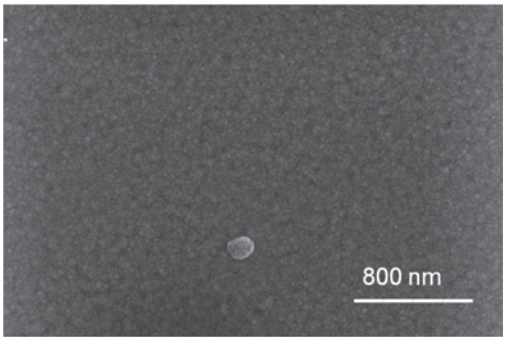

Figure 5.21: SEM image of a $Fe : SnO_2$ surface deposited on gold. Magnitude: 100000, EHT: 10 kV

The $Fe : SnO_2$ layers have been deposited with different thicknesses (5, 10, 50 and 100 nm) on Si in order to investigate them by SE mapping. The applied general model to fit the generated data to the experimental data consisted of (top to bottom):

$Fe : SnO_2$ (one Tauc-Lorentz)
silicon [53]

In Figure 5.22, the dispersion of the optical constants for a 5 nm $Fe : SnO_2$ layer on Si is shown .

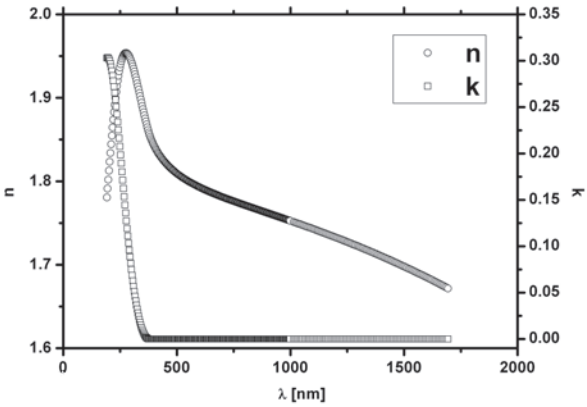

Figure 5.22: Optical constants of a Fe : SnO_2 layer on Si

Values for the index of refraction have been found in literature only for undoped SnO_2, which depend on different parameters: Calculation showed that it decreases with the increase of void density (n_{600} = 1.8-2.05) [80]. For radio frequency sputtered SnO_2, it was found that n depends on the stoichiometry: it decreases with increasing concentration of Sn (n_{600} = 1.7-1.9) [81]. When the material is produced by chemical vapour deposition, n depends on deposition temperature (n_{600} = 1.95-2.1) [82]. Furthermore, investigations on thermal evaporation produced SnO_2 (amorphous) and by spray deposition SnO_2 (crystalline) showed that the index of refraction depends on the film thickness. The thicker the film, the lower n is (n_{600} = 1.7-2.0), with low difference between crystalline and amorphous structure [83]. The value determined for iron doped SnO_2 (n_{600} = 1.8) fits well with the values listed above. Based on these results, the optical constants as well as the layer thickness were determined for Fe : SnO_2 layer deposited on gold which were applied for gas sensing. The thickness of the sensing layers was determined dependent on the measuring spot to 8-14 nm.

5.4.2 Experimentally determined SPR effect

Top-coating a gold layer with the $Fe : SnO_2$ material causes a shift of the SPR effect of 2° to higher AOIs (see Figure 5.23), which is high compared to the other coating material (1.5° at most). This is due to the slightly greater thickness of the $Fe : SnO_2$ layers. The stability of the layer, for at least a few weeks, could be proved (see Figure 5.23). The position of the SPR curve shifted slightly after one month, but this is within the range of the measurement uncertainty due to marginal surface irregularity.

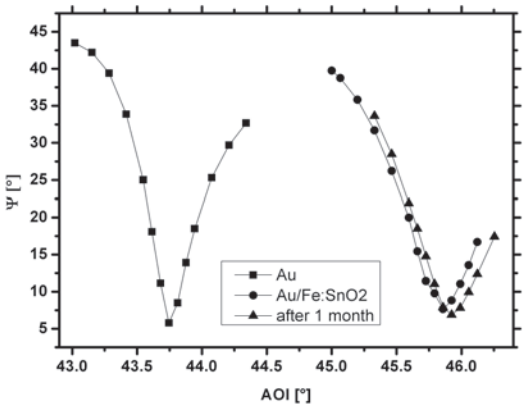

Figure 5.23: Shift of the SPR effect on gold by top-coating with $Fe : SnO_2$ and ageing of the layer

5.4.3 Gas sensing

Gas sensing measurements were performed using fixed AOI measurements. It was observed, that the progression of the measured value Δ is asymptotic when switching to another gas or gas concentration. The mechanisms responsible for gas sensing taking place on this sensor surface are due to the properties of the semiconductor and the doping and are discussed in the following analysis. SnO_2 is widely used in metal oxide semiconductor (MOS) gas sensors,

which detect the resistance change when gases are catalytically oxidised by oxygen ions adsorbed on the sensor surface [11, 12]. For example, methane is converted to carbon dioxide, water and excess electrons, which are responsible for the change in resistance. The generated water molecules damp this effect, since they can react with the metal and oxygen atoms at the lattice position and create a vacancy, which neutralises the excess charges [13]. The products carbon dioxide and water desorb and are released in the ambient atmosphere. These surface reactions normally run at temperatures between 200 ℃ and 250 ℃ [11]. In the measurements performed at room temperature and presented here, the reactions could be promoted by the energy deposition of the laser and the resulting higher temperature on the measurement spot. The mechanism responsible for gas sensing on the $Fe : SnO_2$ sensor layer is thus the coordination of:

- the change of index of refraction in the gas phase
- the formation of an adsorbed layer
- the diffusion of the gas into the layer
- the solvatation of the gas in the layer
- the catalytic oxidation of the adsorbed analyte gas
- the change of index of refraction in the gas phase by the released products

The lowest detectable concentrations (LDC) have been determined for selected analyte gases, which are summarised in Table 5.4. The material is sensitive to low concentrations: they are of the same magnitude as for the other materials.

Table 5.4: Lowest detected concentrations (LDC) of selected gases on Fe:SnO_2

Gas	LDC [ppm]
Methane	10
Propane	10
Carbon dioxide	100
Hydrogen	5

The gas sensing measurements on this sensor layer demonstrated a special aspect: the material shows an extreme high sensitivity to the toxic gas carbon monoxide (CO). The lowest detected value is so far 5 ppm hydrogen with any material and here a carbon monoxide concentration lower than 1 ppm could be detected. Even 0.5 ppm of the gas causes a clear shift of 0.2° in Δ, see Figure 5.24. The sensitivity to CO is based on the different mechanisms taking place on the surface described above. The change of index of refraction and adsorption on the surface are part of it, furthermore the catalytic oxidation of the analyte gas which contributes to the gas sensitivity. The main reaction in this case is the conversion of CO with an adsorbed oxygen ion to carbon dioxide and excess charges. In contrast to the oxidation of methane, no water molecules, which damp the effect of the excess charges, originate [13]. Moreover, the CO molecules can easily be linked to iron ions, as in iron carbonyl complexes [84, 85]. The complex compounds cause a change in the refractive index of the top-layer and the surface bonded CO molecules are catalytically oxidised to carbon dioxide, which desorbs and contributes to the change in the refraction index of the gas phase. The different particles which influence the refractive index are in steady state: complexes, excess charges, carbon monoxide, and carbon dioxide.

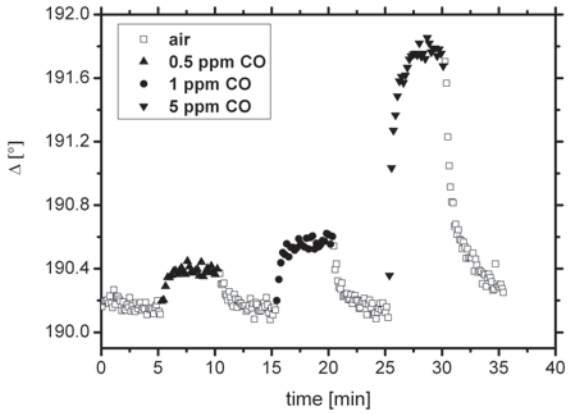

Figure 5.24: Detection of carbon monoxide in the low ppm range on Fe : SnO_2 top-coated on Au

To illustrate the special response of the Fe : SnO_2 layer to CO, the LDCs of this toxic gas on the investigated sensor materials are compared in Table 5.5. The other materials show an improvement in CO detection compared to unprotected gold, but the LDCs are three orders of magnitude higher than for Fe : SnO_2.

Table 5.5: Lowest detected concentrations (LDC) of CO on different materials

Material	LDC of CO [ppm]
Au	1000
TiO_2	100
ZrO_2	500
MgF_2	100
Fe : SnO_2	0.5

Thin Fe : SnO_2 layers have proved their applicability as sensing material for low concentrations of gases, especially to the toxic gas carbon monoxide. This one has to be detected in some industrial applications in concentration ranges of < 1ppm [1], which can be achieved with Fe : SnO_2 as sensor material.

The very special sensitivity to carbon monoxide means a first step towards selectivity of the sensor system.

5.5 Comparison of top-coating materials

In the prior sections, several materials for the top-coating of the gold layers have been introduced: PVD and SG TiO_2, ZrO_2, MgF_2 and $Fe:SnO_2$. All materials are in the same thickness range within 3 - 10 nm and show a closed structure except ZrO_2, which has an isles structure. No difference concerning the stability was observed: All materials are physically stable for at least one month and chemically stable against the investigated gases. Furthermore, it is possible to detect low gas concentrations. The detection limits for Au and Au top-coated with the accordant materials are summarised in Table 5.6. The gold sensor is sensitive to the hydrocarbons and hydrogen under their LEL. The lower value for hydrogen is due to the small hydrogen molecules, which are able to penetrate the gold. The formation of an adsorbed layer is promoted in case of the polar gas carbon monoxide and thus the detection limit is lower compared to the non-polar gases. The top-coating materials reduce the detection limits significantly. TiO_2 and ZrO_2, both produced by the SG process show similar sensitivity, whereas PVD TiO_2 yielded higher detection limits. The production process determines the pore volumes and accessible surface areas of the adsorbent. The different detection limits could also be due to the different chemical structure. The low calcination temperature of SG TiO_2 leads to the non-quantitative release of water and hydroxyl groups remain which can attract the analyte gas by forming hydrogen bridge bonds.

The lower values for methane compared to propane (for all materials except MgF_2) can be explained by the molecule area of the adsorbate. Methane is a smaller molecule with an area of $\sim$ 16 Å^2, than propane with an area of $\sim$ 28 Å^2 [86] and can thus penetrate the layer easier. The values for the detection limits contain an uncertainty due to the surface inhomogeneity. It cannot be excluded that for another measuring spot lower concentrations would be stated. This could be an explanation for the exception of MgF_2 concerning the value for methane. Although the area of carbon dioxide is between methane

and propane ($\sim$ 19 Å^2), all materials yielded higher detection limits for this gas. This could be due to the different molecule symmetry: methane and propane are nearly spherical, carbon dioxide is linear. Furthermore, hydrogen bridge bonds play a role: in the case of the hydrocarbons, hydro bridge bonds between the hydrogen atoms of the analyte gas and the oxygen or fluoride atoms are formed in the sensor layer respectively. The gas molecules are thus attracted near the surface. In case of carbon dioxide, no hydrogen bridge bonds are formed.

As the values for ZrO_2 are similar to SG TiO_2, it is concluded that the SG process in combination with low calcination temperatures produces layers which are ideal for sensing gas due to their large surface areas, which allows the formation of an adsorption layer and low density, which allows pore diffusion.

The sensitivity of $Fe : SnO_2$ to carbon monoxide is noticeable. Although the values for the hydrocarbons are lower than for the other materials, the sensitivity to carbon monoxide is a sign for selectivity, since the other materials do not response significantly. This is obviously due to the doping of the SnO_2.

Table 5.6: Comparison of LDCs of selected gases for Au and top-coated Au sensor systems. 1: PVD, 2: SG

Gas	LDC [ppm]					
	Au	TiO_2[1]	TiO_2[2]	ZrO_2	MgF_2	$Fe : SnO_2$
Methane	2000	90	15	15	100	10
Propane	2500	120	50	50	50	10
Hydrogen	700	25	5	15	5	5
Carbon dioxide	8500	170	85	85	150	100
Carbon monoxide	1000	100	100	500	100	0.5

5.6 Installation of the sensor system at a gas pipe

In order to investigate the sensor system in regard to creating a feasible application in industry, a gold layer top-coated with TiO_2 was directly deposited on a 8 mm x 10 mm BK7 prism, which was adapted to a stainless steel tube (diameter 9 mm) as used in commercial gas pipelines. The sensor behaviour in the tube was observed to be comparable to the measuring cell concerning the response of Δ and the detection limits, and in addition, some measurements with interesting results could be performed. Due to the regular shape of the tube in comparison to the measuring cell, the analyte gases were expected to disperse regularly, particularly when dosed in short pulses. Pulse measurements are also used in residence time studies for continuous chemical reactors, since they give information about the substrate dispersion and diffusion behaviour [87]. In Figure 5.25, the results of an experiment with helium pulses is shown. Nitrogen (100 % (v/v)) is used as reference gas and after 6 minutes, helium (100 % (v/v)) is dosed for 5, 30, 60, and 180 s respectively. In order to compare the experiments, the graphs have been vertically arranged. The 5 s impulse of helium causes a peak to lower Δ values as expected due to the difference in index of refraction. The shape of the peak describes the dispersion of the gas in the tube. After opening the valve, the gas needs some time to flow through the tube until reaching the sensor. The concentration profile shows a distribution with a few atoms at the beginning and the end and the main part in the middle. By expanding the pulse time to 30 s, the peak gets wider and bigger since more gas is released and a higher concentration gets in touch with the sensor. In the progression of the pulse with 60 s length, there is an interesting difference to the prior pulses: The Δ values decrease quickly, but then they rise and a little plateau is formed. This plateau is more obvious in the 180 s pulse and can be explained as follows: Δ reacts to the change of index in refraction in the gas phase which happens when the helium atoms replace the nitrogen molecules. After a certain pulse time, the residence time is high enough so that the helium atoms have time to diffuse into the top-layer and to be adsorbed. The optical constants of the material change, the index of refraction increases and thus the Δ values, which counteracts the effect of

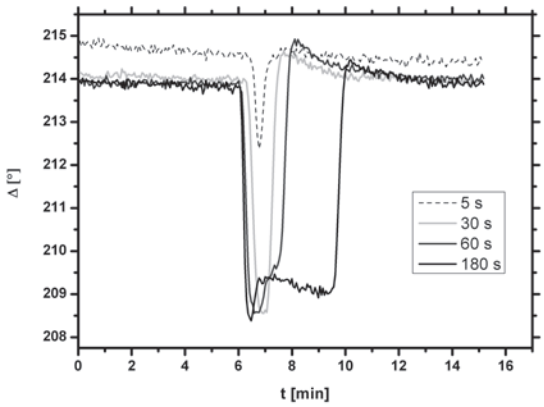

Figure 5.25: Helium (100 % (v/v)) pulses with different duration and nitrogen (100 % (v/v)) as reference gas detected on a TiO_2 layer on Au

the index change in the gas phase. After the helium pulse, the determining factor is again the change of the index of refraction in the gas phase. The high concentration of the nitrogen molecules causes the quick increase in Δ, but the helium atoms are still adsorbed in the layer. This indicates the increase of the values over the base line: both, index of refraction in the gas phase and index of refraction of the top-layer cause a deflection of Δ in the same direction. The helium atoms desorb and thus the Δ values reach the initial value quickly. The result shows that in case of gases with lower index of refraction than the reference gas, the different mechanism which are responsible for gas sensing (compare Section 5.1) can counteract and the response in Δ is reduced. This fact must be considered when choosing the reference gas. The same measurement was performed with methane, a gas with higher refractive index than nitrogen (data not shown). In this case, the change in the gas atmosphere and the diffusion of the gas into the layer both cause an increase in Δ, the signal is thus enforced.

Further investigations were made concerning the pressure sensitivity of the sensor. The pressure inside the tube was varied using a throttle valve. In

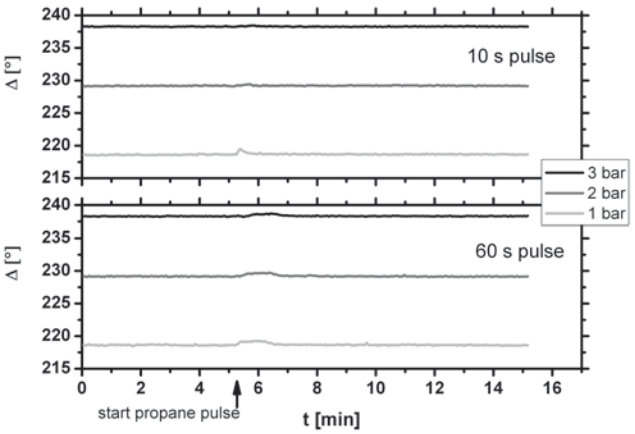

Figure 5.26: Propane (100 % (v/v)) pulses with nitrogen (100 % (v/v)) as reference gas at different pressures on a BK7/Au/TiO_2 system in a tube

Figure 5.26, the sensor response to propane (100 % (v/v)) pulses with nitrogen (100 % (v/v)) as reference gas under different pressures is shown. The pulses had different durations (10 and 60 s) and were set 5 min after the start of the measurement. The higher the pressure, the higher the Δ value, which is easy to understand: the gas atmosphere is densified and the gas molecules pressed into the sensitive layer. A 10 s pulse of propane clearly causes a visible peak at normal pressure, but at higher pressures, it is not distinguishable from the base line. Only when the pulse duration is prolonged, can the propane be detected. This pressure dependence must be considered in a probable application of the sensor system: the signal is dependent on the pressure and slight changes in concentration could be missed.

6 Summary

In this work, a new method to detect all types of gas has been developed and investigated. The sensor system is based on surface plasmon resonance (SPR) effect with ellipsometric read-out. The Kretschmann configuration with a BK7 glass prism on a BK7 slide coated with a 40 - 50 nm gold layer was used. Several methods for surface investigation were applied: scanning electron microscopy, atom force microscopy and spectroscopic ellipsometry mapping. It was found that the gold surfaces have a relatively smooth microstructure with an average roughness of 1.3 nm and the thickness varies between 1-2 nm. The small inhomogeneity leads to the individuality of every measuring spot and the difficulty of performing reproducible experiments. The dependence of the SPR effect on the angle of incidence (AOI) was simulated before starting the experiments and based on the results the AOI range was chosen. AOI spectra of the ellipsometric angles Ψ and Δ were taken in nitrogen or synthetic air atmospheres respectively. Repeating the experiment in another gas atmosphere (e.g. pure methane, propane or helium) resulted in a shift of the location of the SPR effect, depending on the refractive index to higher or lower AOIs relative to the reference gas (nitrogen or air). Since Δ is more sensitive than Ψ, it was used in time dependent measurements: an AOI in the most sensitive region was fixed and Δ was quantified every 3.5 s. With this fixed AOI measuring method, the detection of small concentrations was possible. The analyte gases were diluted with the reference gas and flowed alternately with it through the measuring cell. The gases caused, dependent on their type and concentration, an abrupt peak in Δ to higher or lower values. It was observed, that polar gases cause a different behaviour of Δ than non-polar gases: the increase or decrease run slower and approximated a plateau. Therefore, the principle of gas detection was assumed to be based on the change of the refractive index

in the gas atmosphere and in the formation of an adsorbed layer. The lowest detectable concentrations were determined for selected gases, which ranged between 700 ppm for hydrogen and 8500 ppm for carbon dioxide. The gas detection on gold has two disadvantages: the first is the contamination of the gold layer with sulphuric compounds in the laboratory atmosphere, which could be affirmed by experiments with hydrogen sulfide. The continuous contamination is observed in the Ψ- and Δ- AOI spectra as an irreversible shift of the location of the SPR effect and in the fixed AOI measurements as an omnipresent small drift in the Δ values. The second disadvantage is the detection limits, which are not low enough for some probable applications e.g. the detection of toxic gases. Therefore, the gold layers were coated with thin additional layers. Inorganic materials were chosen as top-coating layers due to their chemical stability and the possibility of depositing them in extremely thin layers (5-10 nm). As protective layers as well as an enhancement for the sensor sensitivity, TiO_2, ZrO_2, MgF_2, and $Fe : SnO_2$ proved of value. The TiO_2 layers were produced by physical vapour deposition (PVD) as well as by sol-gel (SG) process. The surface investigation yielded a microstructure in the PVD layers and absolutely flat SG layers. TiO_2 protects the gold layer from contamination, as proven by hydrogen sulfide experiments. The fixed AOI measurements resulted in Δ curves similar to adsorption curves and the lowest detected gas concentrations were determined at 90 ppm methane and at 25 ppm hydrogen for PVD layers, at 15 ppm methane and at 5 ppm hydrogen for SG layers. The sensing mechanism is assumed to be based on a interaction of different mechanisms: change of the refractive index in the gas phase, formation of an adsorbed layer (the surface area and hence the adsorption area is enlarged compared to uncoated gold), the diffusion of the gases in to the layer, the solvation of the gas inside the layer and catalytic reactions on the surface. The higher sensitivity of SG layers could be caused by the lower density of the material and the different chemical structure. Top-coating the gold with SG ZrO_2, SG MgF_2 or $Fe : SnO_2$ resulted in similar results: all layers protected the gold from contamination and sensitivity was enhanced.

$Fe : SnO_2$ is selective to the toxic gas carbon monoxide due to the doping: iron - carbon monoxide complexes are formed and the catalytic oxidation to carbon dioxide follows. 0.5 ppm carbon monoxide was detected. PVD TiO_2 layers were used to perform experiments in a tube set-up to investigate the sensor behaviour in a probable industrial application. With this tube configuration pulse experiments were performed, which confirmed the coexistence of several mechanisms. Furthermore, experiments concerning pressure dependence of the sensor were also performed.

7 Conclusions and outlook

SPR enhanced ellipsometry is in principle a feasible system for sensing gas. Using fixed AOI with gold layers allows detection of concentrations in the low % region which is enough to detect e.g. hydrocarbons under their LEL. Regarding response and relaxation time, the sensor system is extremely fast. As soon as any change in the gas atmosphere occurs, it becomes apparent in the Δ values. Therefore, an application in the field of explosion protection is theoretically imaginable . However, the loss in sensitivity and the resulting drift in the base line due to the contamination on freshly deposited gold must be considered. On aged gold layers, which are saturated with sulphide, the base line is stable, but the sensitivity is reduced. In practice, a frequent cleaning and recalibration would be required, which is laborious and not useful. By using top-coated gold layers, the sensor is stable on the one hand and sensitive enough on the other hand, whereas the sensitivity depends on the production process of the top layer. In further investigations, the process parameters could be varied to achieve different surface qualities and to determine the effect on the sensitivity. Also, other depositing processes like atomic layer deposition could be applied to investigate the influence of the process on the interaction with gases or to discover a material which shows specificity towards a certain gas. A sensor system with top-coated gold layers could be applied in the field of explosion protection (detecting flammable gases under their LEL) or in threshold limit value monitoring (detecting harmful gases in concentrations in accordance with particular requirements). Fact is, an ambient air monitoring is not possible with this system at the moment and will never be possible due to cross sensitivity. The sensor responses to any change in the atmosphere as pressure fluctuations, dust particles, air humidity etc. However, the sensor system is locally flexible and therefore easy to adapt to

any procedural devices such as pipelines, reactors or vessels. Furthermore the sensor is minimally invasive, the contact area only needs to be 1 - 2 mm^2. An imaginable application in industry is therefore the in-situ monitoring in chemical plants, e.g. in the feed or bottom stream. The system has to be calibrated to a certain gas in a certain concentration and it must be ensured to fix the measuring spot due to the results of the surface investigations. Very often, gas mixtures are present in industrial processes, but distinguishing gas types is not yet possible as the sensor responds to any concentration change. A first step towards selectivity concerning carbon monoxide was achieved by applying $Fe : SnO_2$, whereas further investigations would be necessary such as the modification of the iron content to investigate its influence on the sensitivity. In order to distinguish the gases, different areas with different sensor materials or several sensors in series could be installed, respectively. For example, a mixture of carbon monoxide and any other gas is present. Two sensors are connected in series, one is $Fe : SnO_2$ and calibrated to the carbon monoxide concentration, the other is any other material, calibrated to the other gas. Any change in the carbon monoxide concentration is registered by the first sensor. The second sensor does not respond at all if the change is too marginal, or the deflection is slighter. In order to apply the sensor system in this way in future, the construction of a more cost-effective prototype with a fixed AOI and a simpler read-out would be the next step. At the moment, the experimental configuration is expensive due to the varied angle ellipsometer. Imaginable is also an application for special requirements in laboratories, where very low concentrations are dealt with, e.g. the concentration determination of gases metabolized by bacteria [88, 89].

The basic principle for detecting gas with surface plasmon resonance enhanced ellipsometry is shown in this work and with further investigation, applications in different areas are possible.

Bibliography

[1] Bhoga, S. S. and Singh, K. Electrochemical solid state gas sensors: An overview. Ionics, 13 (2007) (6):417–427

[2] Hulanicki, A., Glab, S., and Ingman, F. Chemical Sensors Definitions and Classification. Pure and Applied Chemistry, 63 (1991) (9):1247–1250

[3] Homola, J., Yee, S. S., and Gauglitz, G. Surface plasmon resonance sensors: review. Sensors and Actuators B-Chemical, 54 (1999) (1-2):3–15

[4] Nylander, C., Liedberg, B., and Lind, T. Gas-Detection by Means of Surface-Plasmon Resonance. Sensors and Actuators, 3 (1982) (1):79–88

[5] Gründler, P. Chemische Sensoren. Springer-Verlag, Berlin Heidelberg New York (2004)

[6] Piliarik, M. and Homola, J. Surface plasmon resonance (SPR) sensors: approaching their limits? Optics Express, 17 (2009) (19):16505–16517

[7] Arwin, H., Poksinski, M., and Johansen, K. Total internal reflection ellipsometry: principles and applications. Applied Optics, 43 (2004) (15):3028–3036

[8] Chien, F. S. S., Wang, C. R., Chan, Y. L., Lin, H. L., Chen, M. H., and Wu, R. J. Fast-response ozone sensor with ZnO nanorods grown by chemical vapor deposition. Sensors and Actuators B-Chemical, 144 (2010) (1):120–125

[9] Izu, N., Shin, W., Murayarna, N., and Kanzaki, S. Resistive oxygen gas sensors based on CeO2 fine powder prepared using mist pyrolysis. Sensors and Actuators B-Chemical, 87 (2002) (1):95–98

[10] Sooknoi, T., Jadsadapattarakul, D., Thanachayanont, C., and Nukeaw, J. Improved selectivity, response time and recovery time by [010] highly preferred-orientation silicalite-1 layer coated on SnO(2) thin film sensor for selective ethylene gas detection. Sensors and Actuators B-Chemical, 144 (2010) (1):73–80

[11] Graf, M., Barrettino, D., Taschini, S., Hagleitner, C., Hierlemann, A., and Baltes, H. Metal oxide-based monolithic complementary metal oxide semiconductor gas sensor microsystem. Analytical Chemistry, 76 (2004) (15):4437–4445

[12] Barsan, N. and Weimar, U. Conduction model of metal oxide gas sensors. Journal of Electroceramics, 7 (2001) (3):143–167

[13] Rani, S., Roy, S. C., and Bhatnagar, M. C. Effect of Fe doping on the gas sensing properties of nano-crystalline SnO2 thin films. Sensors and Actuators B-Chemical, 122 (2007) (1):204–210

[14] Oehme, F. Chemische Sensoren heute und morgen. expert Verlag, Renningen-Malmsheim (1994)

[15] Yang, D. F., Lu, H. H., Chen, B., and Lin, C. W. Surface Plasmon Resonance of SnO2/Au Bi-layer Films for Gas Sensing Applications. Sensors and Actuators B-Chemical, 145 (2010) (2):832–838

[16] Agbor, N. E., Cresswell, J. P., Petty, M. C., and Monkman, A. P. An optical gas sensor based on polyaniline Langmuir-Blodgett films. Sensors and Actuators B-Chemical, 41 (1997) (1-3):137–141

[17] Manera, M. G., Leo, G., Curri, M. L., Cozzoli, P. D., Rella, R., Siciliano, P., Agostiano, A., and Vasanelli, L. Investigation on alcohol vapours/TiO2 nanocrystal thin films interaction by SPR technique for sensing application. Sensors and Actuators B-Chemical, 100 (2004) (1-2):75–80

[18] Homola, J. Optical-Fiber Sensor-Based on Surface-Plasmon Excitation. Sensors and Actuators B-Chemical, 29 (1995) (1-3):401–405

[19] Kabashin, A. V., Patskovsky, S., and Grigorenko, A. N. Phase and amplitude sensitivities in surface plasmon resonance bio and chemical sensing. Optics Express, 17 (2009) (23):21191–21204

[20] Fujiwara, H. Spectroscopic Ellipsometry-Principles and Applications. Maruzen Co. Ltd, Tokyo, Japan, Chichester, England (2007)

[21] Hecht, E. Optik. Oldenbourg Verlag Muenchen, Muenchen, 5 edition (2009)

[22] Azzam, R. and Bashara, N. Ellipsometry and polarized light. Elsevier, Amsterdam (1996)

[23] Maxwell, J. C. A Dynamical Theory of the Electromagnetic Field. Philosophical Transactions of the Royal Society of London, 155 (1865):459–512

[24] Drude, P. Lehrbuch der Optik. S. Hirzel (1900)

[25] Daniel, H. Physik 3, Optik-Thermodynamik-Quanten. Walter de Gruyter, Berlin, New York (1998)

[26] Yeh, P. Optical waves in layered media. Wiley (1988)

[27] Raether, H. Surface Plasmons on Smooth and Rough Surfaces and on Gratings. Springer Verlag, Berlin Heidelberg (1988)

[28] Kittel, C. Introduction to solid state physics. Wiley, New York, 7th edition (1996)

[29] Arwin, H., Poksinski, M., and Johansen, K. Enhancement in ellipsometric thin film sensitivity near surface plasmon resonance conditions. Physica Status Solidi a-Applications and Materials Science, 205 (2008) (4):817–820

[30] Sambles, J. R., Bradbery, G. W., and Yang, F. Z. Optical-Excitation of Surface-Plasmons - an Introduction. Contemporary Physics, 32 (1991) (3):173–183

[31] Kretschmann, E. and Raether, H. Radiative Decay of Non Radiative Surface Plasmons Excited by Light. Zeitschrift Fur Naturforschung Part a-Astrophysik Physik Und Physikalische Chemie, A 23 (1968) (12):2135–2136

[32] Kern, W. and Puotinen, D. A. Cleaning Solutions BAsed on Hydrogen Peroxide for use in Silicon Semiconductor Technology. RCA Review, 31 (1970):187–206

[33] Krüger, H., Hertwig, A., Beck, U., and Kemnitz, E. Low temperature sol-gel metal oxide and fluoride layer stacks for optical applications. Thin Solid Films, 518 (2010) (21):6080–6086

[34] Krüger, H., Kemnitz, E., Hertwig, A., and Beck, U. Transparent MgF2-films by sol-gel coating: Synthesis and optical properties. Thin Solid Films, 516 (2008) (12):4175–4177

[35] Woollam, J. A., Johs, B., Herzinger, C. M., Hilfiker, J., Synowicki, R., and Bungay, C. L. Overview of Variable Angle Spectroscopic Ellipsometry (VASE), Part I: Basic Theory and Typical Applications (2000)

[36] Kormunda, M. and Pavlik, J. A single target RF magnetron co-sputtered iron doped tin oxide films with pillars. Vacuum, 85 (2011) (9):871–874

[37] Schmidbaur, H., Cronje, S., Djordjevic, B., and Schuster, O. Understanding gold chemistry through relativity. Chemical Physics, 311 (2005) (1-2):151–161

[38] Okumura, M., Nakamura, S., Tsubota, S., Nakamura, T., Azuma, M., and Haruta, M. Chemical vapor deposition of gold on Al2O3, SiO2, and TiO2 for the oxidation of CO and of H-2. Catalysis Letters, 51 (1998) (1-2):53–58

[39] Watkins, J. J., Cabanas, A., and Long, D. P. Deposition of gold films and nanostructures from supercritical carbon dioxide. Chemistry of Materials, 16 (2004) (10):2028–2033

[40] Petri, D. F. S., Wenz, G., Schunk, P., and Schimmel, T. An improved method for the assembly of amino-terminated monolayers on SiO2 and the vapor deposition of gold layers. Langmuir, 15 (1999) (13):4520–4523

[41] Bach, H. and Neuroth, N. The Properties of Optical Glass (Schott Series on Glass and Glass Ceramics), volume 1st ed. 1995. Corr. 2nd printing. Springer Berlin Heidelberg (1995)

[42] Palik, E. D. and Ghosh, G. Handbook of Optical Constants of Solids Five-volume Set: Handbook of optical constants of solids I, II, and III. Academic Press (1998)

[43] Etchegoin, P. G., Le Ru, E. C., and Meyer, M. An analytic model for the optical properties of gold. Journal of Chemical Physics, 125 (2006) (16)

[44] Doremus, R. H. Optical Properties of Small Gold Particles. Journal of Chemical Physics, 40 (1964) (8):2389

[45] Langmuir, I. The Adsorption of Gases on Plane Surfaces of Glass, Mica and Platinum. Journal of the American Chemical Society, 40 (1918):1361–1403

[46] NMP. Chemische Analytik-Nachweis-, Erfassungs- und Bestimmungsgrenze unter Wiederholbedingungen-Begriffe, Verfahren, Auswertung (2008)

[47] Rodriguez, J. A., Dvorak, J., Jirsak, T., Liu, G., Hrbek, J., Aray, Y., and Gonzalez, C. Coverage effects and the nature of the metal-sulfur bond in S/Au(111): High-resolution photoemission and density-functional studies. Journal of the American Chemical Society, 125 (2003) (1):276–285

[48] Flink, S., van Veggel, F. C. J. M., and Reinhoudt, D. N. Sensor functionalities in self-assembled monolayers. Advanced Materials, 12 (2000) (18):1315–1328

[49] Love, J. C., Wolfe, D. B., Haasch, R., Chabinyc, M. L., Paul, K. E., Whitesides, G. M., and Nuzzo, R. G. Formation and structure of self-

assembled monolayers of alkanethiolates on palladium. Journal of the American Chemical Society, 125 (2003) (9):2597–2609

[50] Rybachuk, M., Hertwig, A., Weise, M., Sahre, M., Mann, M., Beck, U., and Bell, J. M. Near infrared optical materials from polymeric amorphous carbon synthesized by collisional plasma process. Applied Physics Letters, 96 (2010) (21):–

[51] Chen, X. and Mao, S. S. Titanium dioxide nanomaterials: Synthesis, properties, modifications, and applications. Chemical Reviews, 107 (2007) (7):2891–2959

[52] Bendavid, A., Martin, P. J., and Takikawa, H. Deposition and modification of titanium dioxide thin films by filtered arc deposition. Thin Solid Films, 360 (2000) (1-2):241–249

[53] Herzinger, C. M., Johs, B., McGahan, W. A., Woollam, J. A., and Paulson, W. Ellipsometric determination of optical constants for silicon and thermally grown silicon dioxide via a multi-sample, multi-wavelength, multi-angle investigation. Journal of Applied Physics, 83 (1998) (6):3323–3336

[54] Langlet, M., Burgos, M., Coutier, C., Jimenez, C., Morant, C., and Manso, M. Low temperature preparation of high refractive index and mechanically resistant sol-gel TiO2 films for multilayer antireflective coating applications. Journal of Sol-Gel Science and Technology, 22 (2001) (1-2):139–150

[55] Tanemura, S., Miao, L., Jin, P., Kaneko, K., Terai, A., and Nabatova-Gabain, N. Optical properties of polycrystalline and epitaxial anatase and rutile TiO2 thin films by rf magnetron sputtering. Applied Surface Science, 212 (2003):654–660

[56] Kanaev, A., Kuznetsov, A. I., Kameneva, O., Alexandrov, A., Bityurin, N., and Chhor, K. Chemical activity of photoinduced Ti3+ centers in titanium oxide gels. Journal of Physical Chemistry B, 110 (2006) (1):435–441

[57] Shelimov, B. N., Lisachenko, A. A., Mikhailov, R. V., Basov, L. L., and Che, M. Photocatalytic reduction of NO by CO on titanium dioxide under visible light irradiation. Journal of Physical Chemistry C, 111 (2007) (39):14440–14447

[58] Hahn, S. H., Kim, D. J., Oh, S. H., and Kim, E. J. Influence of calcination temperature on structural and optical properties of TiO2 thin films prepared by sol-gel dip coating. Materials Letters, 57 (2002) (2):355–360

[59] Dobson, K. D. and McQuillan, A. J. An infrared spectroscopic study of carbonate adsorption to zirconium dioxide sol-gel films from aqueous solutions. Langmuir, 13 (1997) (13):3392–3396

[60] Kukli, K., Ritala, M., Aarik, J., Uustare, T., and Leskela, M. Influence of growth temperature on properties of zirconium dioxide films grown by atomic layer deposition. Journal of Applied Physics, 92 (2002) (4):1833–1840

[61] Navio, J. A., Hidalgo, M. C., Colon, G., Botta, S. G., and Litter, M. I. Preparation and physicochemical properties of ZrO2 and Fe/ZrO2 prepared by a sol-gel technique. Langmuir, 17 (2001) (1):202–210

[62] Mulla, I. S., Niranjan, R. S., and Sathaye, S. D. Bilayered tin oxide : zirconia thin film as a humidity sensor. Sensors and Actuators B-Chemical, 81 (2001) (1):64–67

[63] Ju, H. X., Liu, S. Q., Dai, Z. H., and Chen, H. Y. Immobilization of hemoglobin on zirconium dioxide nanoparticles for preparation of a novel hydrogen peroxide biosensor. Biosensors and Bioelectronics, 19 (2004) (9):963–969

[64] Yang, Y. H., Wang, Z. J., Yang, M. H., Li, J. S., Zheng, F., Shen, G. L., and Yu, R. Q. Electrical detection of deoxyribonucleic acid hybridization based on carbon-nanotubes/nano zirconium dioxide/chitosan-modified electrodes. Analytica Chimica Acta, 584 (2007) (2):268–274

[65] Amberg, M. and Gunter, J. R. Metastable cubic and tetragonal zirconium dioxide, prepared by thermal oxidation of the dichalcogenides. Solid State Ionics, 84 (1996) (3-4):313–321

[66] Khawaja, E. E. and Tomlin, S. G. Optical-Properties of Thin-Films of Tantalum Pentoxide and Zirconium Dioxide. Thin Solid Films, 30 (1975) (2):361–369

[67] Rojas-Cervantes, M., Martin-Aranda, R., Lopez-Peinado, A., and Lopez-Gonzalez, J. ZrO2 optained by the sol-gel method: influence of synthesis parameter on physical and structural characteristics. Journal of materials Science, 29 (1994):3743–3748

[68] Matero, R., Ritala, M., Leskela, M., Sajavaara, T., Jones, A. C., and Roberts, J. L. Evaluation of new aminoalkoxide precursors for atomic layer deposition. Growth of zirconium dioxide thin films and reaction mechanism studies. Chemistry of Materials, 16 (2004) (26):5630–5636

[69] Yussouff, M., Brailsford, A. D., and Logothetis, E. M. A first-principles model of the zirconia oxygen sensor. Sensors and Actuators B-Chemical, 44 (1997) (1-3):321–326

[70] Nenninger, G. G., Tobiska, P., Homola, J., and Yee, S. S. Long-range surface plasmons for high-resolution surface plasmon resonance sensors. Sensors and Actuators B-Chemical, 74 (2001) (1-3):145–151

[71] Garces, I., Aldea, C., and Mateo, J. 4-Layer Chemical Fiber Optic Plasmon-Based Sensor. Sensors and Actuators B-Chemical, 7 (1992) (1-3):771–774

[72] Sridhar, M. and Kumbhare, R. M. Magnesium fluoride catalyzed Knoevenagel reaction: An efficient synthesis of electrophilic alkenes. Catalysis Communications, 9 (2008) (3):403–405

[73] Quesnel, E., Dumas, L., Robic, J. Y., and Pauleau, Y. Characterization of magnesium fluoride thin films deposited by direct electron beam evap-

oration. Journal of Vacuum Science and Technology a-Vacuum Surfaces and Films, 18 (2000) (2):465–469

[74] Kemnitz, E., Wuttke, S., Scholz, G., and Rudiger, S. Variation of sol-gel synthesis parameters and their consequence for the surface area and structure of magnesium fluoride. Journal of Materials Chemistry, 17 (2007) (47):4980–4988

[75] Lavers, C. R., Itoh, K., Wu, S. C., Murabayashi, M., Mauchline, I., Stewart, G., and Stout, T. Planar optical waveguides for sensing applications. Sensors and Actuators B-Chemical, 69 (2000) (1-2):85–95

[76] Morrison, S. R. Selectivity in Semiconductor Gas Sensors. Sensors and Actuators, 12 (1987) (4):425–440

[77] Shimanoe, K. and Yamazoe, N. Theory of power laws for semiconductor gas sensors. Sensors and Actuators B-Chemical, 128 (2008) (2):566–573

[78] Vaishampayan, M. V., Deshmukh, R. G., Walke, P., and Mulla, I. S. Fe-doped SnO2 nanomaterial: A low temperature hydrogen sulfide gas sensor. Materials Chemistry and Physics, 109 (2008) (2-3):230–234

[79] Nooke, A., Beck, U., Hertwig, A., Krause, A., Krüger, H., Lohse, V., Kormunda, M., Pavlik, J., and Steinbach, J. SPR enhanced ellipsometric gas monitoring on thin iron doped tin oxide layers. Sensors and Actuators B: Chemical, 160 (2011):609–615

[80] Goldsmith, S., Cetinorgu, E., and Boxman, R. L. Modeling the optical properties of tin oxide thin films. Thin Solid Films, 517 (2009) (17):5146–5150

[81] Czapla, A., Kusior, E., and Bucko, M. Optical-Properties of Non-Stoichiometric Tin Oxide-Films Obtained by Reactive Sputtering. Thin Solid Films, 182 (1989):15–22

[82] Davazoglou, D. Optical properties of SnO2 thin films grown by atmospheric pressure chemical vapour deposition oxidizing SnCl4. Thin Solid Films, 302 (1997) (1-2):204–213

[83] Demiryont, H. and Nietering, K. E. Structure and Optical-Properties of Tin Oxide-Films. Solar Energy Materials, 19 (1989) (1-2):79–94

[84] Collman, J. P., Brauman, J. I., Halbert, T. R., and Suslick, K. S. Nature of O-2 and Co Binding to Metalloporphyrins and Heme Proteins. Proceedings of the National Academy of Sciences of the United States of America, 73 (1976) (10):3333–3337

[85] Hu, X. L., Obrist, B. V., Chen, D. F., Ahrens, A., Schunemann, V., and Scopelliti, R. An Iron Carbonyl Pyridonate Complex Related to the Active Site of the [Fe]-Hydrogenase (Hmd). Inorganic Chemistry, 48 (2009) (8):3514–3516

[86] Webster, C. E., Drago, R. S., and Zerner, M. C. Molecular dimensions for adsorptives. Journal of the American Chemical Society, 120 (1998) (22):5509–5516

[87] Schwan, P. and Moller, K. P. Analysis of the pulse response in a CSTR for diffusion measurement in bi-porous adsorbent pellets. Chemical Engineering Science, 56 (2001) (8):2821–2830

[88] Engel, R. R., Schwartz, S., Chapman, S. S., and Matsen, J. M. Carbon-Monoxide Production from Heme Compounds by Bacteria. Journal of Bacteriology, 112 (1972) (3):1310

[89] Kopke, M., Mihalcea, C., Bromley, J. C., and Simpson, S. D. Fermentative production of ethanol from carbon monoxide. Current Opinion in Biotechnology, 22 (2011) (3):320–325

List of abbreviations

a_i	ion's activity
AFM	atomic force microscopy
AOI	angle of incidence
α	polarisability
BAM	Bundesanstalt für Materialforschung und -prüfung
BK7	borosilicate glass
B,$\vec{B}$	magnetic induction
c	velocity of light in vacuum
CVD	chemical vapour deposition
χ	dielectric susceptibility
d	thickness
Δ	ellipsometric parameter
$\delta_{s,p}$	initial phases
ϵ	dielectric function
ϵ'	real part of the dielectric function
ϵ''	complex part of the dielectric function
E,$\vec{E}$	electric field
$\vec{E}_0$	amplitude of electric field
$\vec{E}_J$	Jones vector
EHT	extra high tension
E_f	photon energy
f	frequency of light
Γ	damping
I	intensity of light
k	extinction coefficient
K,$\vec{K}$	wave vector

LB	Langmuir-Blodgett
LEL	lower explosive limit
LDC	lowest detected concentration
λ	wavelength
M	Mueller Matrix
MFC	mass flow controller
MOSFET	metal oxid semiconductor field-effect transistor
μ	magnetic permeability
n	refractive index
N	complex refractive index
N_a	Avogadro constant
P	dielectric polarisation
p	pressure
PVD	physical vapour deposition
Π	degree of polarisation
Ψ	ellipsometric parameter
Q	potential of a galvanic cell
Q_0	standard reduction potential of a galvanic cell
$\vec{r}$	position of plane wave
$r_{s,r}$	amplitude reflection coefficient for s- and p-polarised light respectively
R	collective Fresnel coefficient for a three layer system
R_a	average surface roughness
R_g	gas constant
RIU	refractive index unit
ρ	ratio of amplitude reflection coefficients
SAM	self-assembled monolayer
SE	spectroscopic ellipsometry
SEM	scanning electron microscopy
SG	sol-gel
SPR	surface plasmon resonance
SPREE	surface plasmon resonance enhanced ellipsometry
$S_{0,1,2,3}$	Stokes parameter

S_e	Stokes vector
T	temperature
t	time
TEM	transmission electron microscopy
TIRE	total internal reflection ellipsometry
$t_{s,r}$	amplitude transmission coefficient for s- and p-polarised light respectively
θ_i	angle of incidence
θ_r	angle of reflection
θ_t	angle of transmission
v	velocity of light in any medium
ω	angular frequency
XPS	X-ray photoelectron spectroscopy
z_i	ion's valence